RIS-embedded UAVs communications for multi-hop fully-FSO backhaul links in 6G networks

Yalçın Ata, *Senior Member, IEEE,* Anna Maria Vegni, *Senior Member, IEEE,*
and Mohamed Slim Alouini, *Life Fellow, IEEE*

***Abstract*—In the upcoming 6G network, the use of reconfigurable intelligent surface (RIS) is expected to revolutionize wireless communications, providing high data rate, directivity, and extending coverage to skip-zones. This paper presents a detailed analysis on RIS for a fully free-space optical (FSO) ground-to-aerial-to-ground system, by means of single and multiple unmanned aerial vehicles (UAVs). Specifically, we introduce a network architecture suitable for FSO backhaul transmissions, connecting ground stations that are not in Line of Sight (LoS) through RIS-embedded UAVs. We present the derivations of outage probability and bit error rate (BER) in case of single- and two-RIS embedded UAVs FSO paths, and for single and multiple RIS number of elements. Numerical results assess the effectiveness of the proposed system, specifically in case of multiple UAVs and number of RIS elements.**

***Index Terms*—Reconfigurable Intelligent Surfaces, Free Space Optics, Unmanned Aerial Vehicles, Outage Probability, Bit Error Rate, 6G**

I. Introduction

In the next generation wireless networks, one of the main challenges is how to deal with the presence of skip-zones in the targeted areas, due to obstructions and blockages. The concept of Smart Electro-Magnetic Environment (SEME) [1] has been introduced to address this problem, aiming to control and manipulate the signal propagation characteristics to improve the effectiveness, quality, as well as the energy-efficiency of wireless networks.

RISs are one of the main tools adopted in SEME. They are thin devices that can be deployed on walls, buildings, and any other surface, and may be exploited to reflect the incident signal in the direction of dead zones, increase communication coverage, and make the channel smarter and controllable [2]. Specifically, every environmental object can be coated with an artificial thin film of electromagnetic material, which senses the environment and whose response to the radio waves is programmed to optimize the performance [3].

Y. Ata is with the Department of Electrical and Electronics Engineering, OSTIM Technical University, 06374 Yenimahalle, Ankara, Turkey. Email: ylcnata@gmail.com

A. M. Vegni is with the Department of Industrial, Electronics and Mechanical Engineering, Roma Tre University, Rome, Italy. Email: annamaria.vegni@uniroma3.it

M. S. Alouini is with the Computer, Electrical and Mathematical Science and Engineering Division, King Abdullah University of Science and Technology (KAUST), Thuwal 23955-6900, Kingdom of Saudi Arabia. Email: slim.alouini@kaust.edu.sa

RISs are comprised of passive tunable unit cells, which can successfully manipulate and control the electromagnetic waves. Each of the elements comprising a RIS is able to induce a certain phase shift, independently on the incident signal, thus changing accordingly the reflected signal propagation [4]. RIS-assisted wireless communications are then expected to achieve significant performance improvement and coverage enhancement in a cost-effective and energy-efficient manner. This is possible by properly programming the reflection coefficients of RISs unit cells. It follows that RISs allow to create a *smart radio environment* [5], that is a smart reconfigurable space able to redirect and control the electromagnetic signals, thus making more reliable the exchange of data between the transmitters and the receiver, by using low-cost inactive reflecting elements. A detailed overview on the use of RIS to solve various issues, such as channel estimation, transmission design and radio localization, with particular emphasis on the signal processing point of view is presented in [6].

The use of RISs has been largely considered for radio frequency (RF), mmWave communications, and recently also for THz communications [7]. Moving to higher frequencies, approaching the quasi-optical bands, RISs can also be adopted for wireless optics, such as visible light communications (VLC) [8] and FSO [9]. The latter technology, which is the topic of this paper, suffers from atmospheric and weather attenuation, as well as pointing errors, which do not allow a practical design nowadays and cause outages and disconnections. The use of RISs for FSO can overcome such limitations and provide high-effective communications, thanks to the RIS's features of controlling the impinging wireless signals towards a desired target. In this vision, motivated by the necessity of high data rates and reliable links for next generation wireless networks, we aim to exploit RIS-embedded devices for FSO ground-to-aerial connectivity, and vice versa. By adopting UAVs, we can transmit a wireless signal from a ground station to a relay UAV node, in order to overcome possible obstructions *i.e.*, No Line Of Sight, NLoS. Extending to a set of UAVs (*i.e.*, a UAVs swarm), connectivity links may be established via multi-hop propagation among RIS-embedded UAVs. Usually, RISs are considered as relay nodes linking a source to a destination node. In this paper, we are interested in investigating the FSO connectivity path from a ground station to a final destination through a *multi-hop UAV bridge*, established in case of lack of LoS link. Specifically, considering a couple of ground stations, the multi-hop UAV bridge can connect them, thus working as a wireless backhaul communication link [10]. The proposed

RIS-embedded multi-hop UAV path is expected not only to extend the network coverage of a ground station, but also to manage the connectivity links in case of failures.

The main novelty of this paper is the analytical analysis of a fully-FSO multi-hop RIS-embedded path, where we combined the effects of attenuation losses, turbulence, pointing errors, and angle of arrival (AOA) attenuation. This analysis provides the derivation of bit-error-rate (BER) and outage probabilities, which will be supported by numerical and simulation results. To summarize, in this paper we aim to investigate the following goals:

- We present a network architecture for ground-to-aerial-to-ground FSO communications, through the use of one and two RIS-embedded UAV-assisted path;
- Differently from traditional RIS-based wireless communications, where RISs are deployed to connect a transmitter to a final user, in this paper we use the proposed system model for backhaul communications linking a couple of transmitting nodes *i.e.*, base stations;
- We assume fixed aerial devices, such as UAVs in known positions, are equipped with RISs comprised of a variable number of elements. UAVs form a multi-hop path connecting two ground base stations. The UAV network topology is a priori known and nodes are not in a mesh configuration. Then, we present the theoretical analysis of the outage probability, as well as the BER, in case of one and two UAV-assisted paths, under atmospheric and weather attenuation losses;
- From the achieved results, expressed in terms of outage probability and BER that are supported by Monte Carlo simulations and high signal-to-noise ratio (SNR) approximations, we evince the benefits of a multi-RIS-embedded UAV-assisted FSO backhaul path, with high number of RIS elements. The use of multi-hop RIS-embedded UAV paths results as a viable approach for optimal link management.

This paper is organized as follows. Section II deals with some recent works on the use of RISs for FSO. In Section III we introduce the proposed ground-to-aerial-to-ground FSO network architecture, where RIS-embedded UAV devices are used as relay nodes in case of both one- and two-relay nodes. The FSO attenuation losses are also presented. Section IV introduces the channel model in case of single and multiple UAV, which will be then adopted in the derivation of probability density function (PDF) channel state, as detailed in Section V. Finally, in Section VI and VII we will derive the outage probabilities and the expressions of the average BER in case of one- and two- UAV-assisted FSO paths, respectively, while Section VIII presents the asymptotic analysis evaluated in case of high SNR regime, and large number of RIS elements. Numerical results, expressed in terms of outage and BER performances, have been carried out in Section IX, in case of different geometrical factors and number of RIS elements. It will be easy to notice the benefits of multi-hop links, as well as the increasing number of RIS elements can reduce the outage probability. Finally, conclusions are drawn in Section X.

II. Related works

RISs have been largely exploited to enhance connectivity in FSO communication systems, usually in conjunction with RF links. High altitude platform systems (HAPS) are adopted as relay nodes to connect satellite systems and ground stations, by means of hybrid FSO/RF. However, the main drawback of hybrid FSO/RF systems is the limited bandwidth of the RF connection, which causes restricted end-to-end performance.

The use of RISs can enhance the system performance, thanks to their ability to control and manipulate the impinging wireless signal toward a desired destination. For this aim, the work in [11] presents a dual-hop RIS-based hybrid FSO/RF communication system, where an RIS is utilized to improve the coverage and system performance, by smartly tuning the signal reflections. A similar contribution is presented by Chapala and Zafaruddin in [12], where data propagation is extended through a multi-hop RF system assisted by RISs. Phase shift of the RIS can severely degrade the performance of FSO communication systems particularly when high mobility is available and the channel coherence time is short due to environmental conditions. In [13], an uplink RIS aided massive multiple-input multiple-output (MIMO) communication system model was examined using the statistical channel state information (CSI) to compensate the phase shifts produced by RIS elements. An analysis on imperfect CSI (for rapidly and slowly changing CSI conditions) based massive MIMO communication system was performed in [14]. The achieved results showed that different performances are obtained assuming different deployments of RIS, in order to compensate the effect of far-field path loss. Specifically, by deploying RIS near the cell-edge users, a significant performance improvement can be obtained. In [15] Li *et al.* introduced a satellite terrestrial integrated network with hybrid FSO/RF systems, where different operation modes are adopted based on weather conditions and the use of HAPSs and UAVs.

On the other hand, considering a fully-FSO system for ground-to-aerial/satellite connectivity is expected to guarantee higher performance, but some limitations are caused by atmospheric turbulence, pointing errors, AOA fluctuations, and in general attenuation loss, that may cause the skip-zone problem. The topic of integrated ground-air-space FSO system for 6G connectivity is initially investigated in [16], [17], but without exploiting the use of RISs. In [18] Ndjiongue *et al.* investigate the use of a single-element RIS for a fully-terrestrial FSO system, and observed the achieved performance are enhanced when the RIS is deployed near the transmitter. Naik *et al.* [19] propose an RIS-assisted FSO system for mitigating the effects of atmospheric turbulence, pointing errors, and communication system signal blockage, assuming the RIS is composed of multiple elements, which provide better performance.

The use of RIS mounted on UAVs has been largely investigated, due to the benefits that are derived [20]. Indeed, an RIS mounted on a UAV acts like a mobile base station that transmits data where a physical installation of the base station is not possible (*e.g.*, in harsh environments). In [21], Jia *et al.* have considered a RIS-mounted UAV for FSO communication links, assuming atmospheric turbulence and pointing error loss

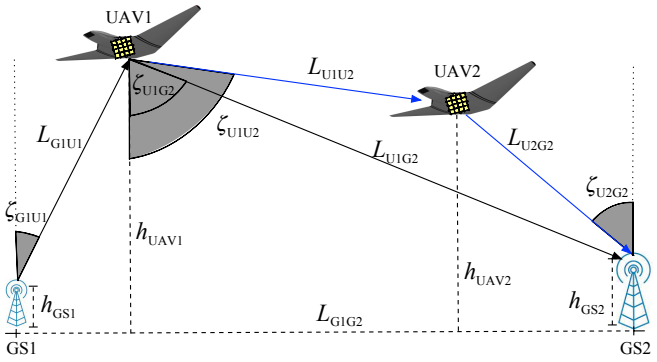

Fig. 1. RIS-assisted FSO ground-air-ground backhaul link. The first path refers to transmission links from GS1 to UAV1, and from UAV1 to GS2. The second path refers to transmission links from GS1 to UAV1, from UAV1 to UAV2, and from UAV2 to GS2.

caused by UAV vibrations. In [22], Luo *et al.* presented a RIS-mounted UAV aided system aiming to both communication and positioning for ground vehicles. In [23] Hanbay and Altin exploit the use of RIS-embedded UAVs, acting as a relay node for the improvement of the network coverage. Such a scenario is designed to prevent obstacles between the transmitter and the receiver, thus ensuring uninterrupted communication. A similar approach is adopted in [24] by Nguyen *et al.* that present a satellite–aerial–ground integrated network where RIS-embedded UAVs are deployed to reflect the signals from the HAPS. Finally, Liqiang *et al.* [25] investigate the use of RIS composed by a large number of reconfigurable passive elements. It was demonstrated that a higher number of reflecting elements can enhance the system performance. It can be noticed that there are several variables impacting the UAV's power consumption and performance, such as the aerodynamic layout and UAV steadiness, as well as the atmospheric attenuation. It has been shown that, on average, UAVs are able to fly with a sensor payload, *e.g.*, camera and GPS device, for about 30 minutes with a fully-charged battery. In order to reduce the energy consumption, solutions to prevent battery outage should be considered [26]. However, this paper considers large UAVs laying at fixed positions, put on air to extend coverage by accordingly redirecting the wireless signal, transmitted by a ground base station to the RIS-equipped UAV, toward a desired destination.

Differently from the above works, in this paper we focus on a fully-FSO system supported by the use of multiple UAVs for backhaul data transmission. To make our study realistic as much as possible, and to move existing works step further, we combined the effects of attenuation losses, turbulence, pointing errors, and AOA attenuation. We will demonstrate that the use of multiple RIS-embedded UAVs, with multiple passive elements, presents lower outage probability and BER, as compared to the case of a single RIS-embedded UAV with a low number of passive elements.

III. System Model

Let us consider the scenario depicted in Fig. 1, where two ground stations (GSs) *i.e.*, GS1 and GS2, are deployed at a distance L_{G1G2} [m]. Without loss of generality, we assume GS1 acts as a transmitter and GS2 as a receiver. UAV devices can be used to relay data connectivity in the air, in case that GS1 and GS2 are not in visibility due to some obstruction (*i.e.*, No Line-of-Sight). Through the use of flying devices, it will be possible to connect the two ground stations, and then to provide a backhaul connectivity link.

As depicted in Fig. 1, we assume multiple UAVs can be used to connect GS1 to GS2, thus providing a multi-hop backhaul path (see black and blue links). Furthermore, UAVs are RIS-embedded, thus allowing to control the impinging FSO signals coming from the ground station GS1 or from the UAVs. Specifically, we assume UAV1 and UAV2 are equipped with number of N and M RIS elements, respectively.

According to the schematic in Fig. 1, we assume that GS1 and GS2 have heights of h_{GS1} [m] and h_{GS2} [m], respectively. Similarly, UAV1 and UAV2 are flying at quotes h_{UAV1} [m] and h_{UAV2} [m], respectively, serving as relay nodes. The FSO connectivity links from GS1 to UAV1 (*i.e.*, L_{G1U1} [m]), from UAV1 to UAV2 (*i.e.*, L_{U1U2} [m]), from UAV1 to GS2 (*i.e.*, L_{U1G2} [m]), and from UAV2 to GS2 (*i.e.*, L_{U2G2} [m]) are all in line of sight (LoS). Finally, we define ζ_{G1U1}, ζ_{U1G2}, ζ_{U1U2}, and ζ_{U2G2} as the zenith angles for the link between GS1 and UAV1, UAV1 and GS2, UAV1 and UAV2, and UAV2 and GS2, respectively.

We assume all the FSO links are affected by multiple attenuation losses due to (*i*) atmospheric turbulence, (*ii*) atmospheric attenuation, (*iii*) the pointing error, and (*iv*) the errors caused by AOA fluctuations. Then, the total loss that the optical beam is exposed will be the combination of above-mentioned phenomena. The expressions of these attenuation loss contributions are derived as follows.

Atmospheric Attenuation: according to the Beer-Lambert law, attenuation loss due to the absorption and scattering effects in atmospheric medium can be given as $h_{al} = e^{-C(\lambda)L}$, where C is the attenuation coefficient that is dependent on the wavelength λ [nm], and L [m] is the link length for optical communication systems, where specific values refer to the links in Fig. 1. The attenuation coefficient is expressed as a function of visibility [27] *i.e.*, $C(\lambda) \simeq \frac{3.912}{V}\left(\frac{\lambda}{550}\right)^{-q}$, where V [km] is the visibility, and the parameter q is given by Kim model [27].

Atmospheric Turbulence: we assume the Hufnagel-Valley (HV) model, for which the turbulence structure constant is empirically found in [28]. Being valid for weak, moderate and strong turbulence conditions, the scintillation index for wide range of turbulence regimes can be found by [28] (pp. 420) *i.e.*, $\sigma_I^2 = \exp\left[\sigma_{\ln X}^2\left(D_G\right) + \sigma_{\ln Y}^2\left(D_G\right)\right] - 1$, where D_G [m] is the aperture diameter, $\sigma_{\ln X}^2$ and $\sigma_{\ln Y}^2$ are the large-scale and small-scale log-irradiance variances, respectively [28].

In this paper, we model the atmospheric turbulence induced fading according to the recently introduced Fisher Snedecor $\mathcal{F}$ atmospheric turbulence model [29], which is statistically suitable for all atmospheric turbulence conditions and yields better fit to experimental data. The PDF of the turbulence channel state h_{at} for $\mathcal{F}$-turbulence channel model is [29]

$$f_{h_{at}}(h_{at}) = \frac{a^a\left(b-1\right)^b h_{at}^{a-1}}{\mathfrak{B}\left(a,b\right)\left(a h_{at}+b-1\right)^{a+b}}, \tag{1}$$

where $\mathfrak{B}(\cdot,\cdot)$ is the Beta function, and the parameters a and b are respectively,

$$a = \frac{1}{\exp(\sigma^2_{\ln Y}) - 1}, \quad \text{and} \quad b = \frac{1}{\exp(\sigma^2_{\ln X}) - 1} + 2. \quad (2)$$

Pointing error: also known as beam misalignment of propagating optical beam in FSO communication link through the atmospheric turbulence, it refers to the deviation of the transmitted optical beam's centroid or focal point from its direction at the receiver plane [28]. This deviation emerges due to the random fluctuations induced by atmospheric turbulence along the optical beam's propagation path. The PDF of the pointing error loss *i.e.*, h_{pl}, is obtained in its integral form as [30]

$$f_{pl}(h_{pl}) = \frac{\eta_s^2}{2\pi q_H} \int_{-\pi}^{\pi} \frac{h_{pl}^{\eta_s^2\xi(\varphi)-1}}{A_0^{\eta_s^2\xi(\varphi)}} d\varphi, \quad (3)$$

where η_s is given as $\eta_s = \omega_e/(2\sigma_s)$, with $\omega_e = \omega_b \left[\sqrt{\pi}\,\mathrm{erf}(\nu)/(2\nu\exp(-\nu^2))\right]^{1/2}$, $\mathrm{erf}(\cdot)$ as the error function, $\nu = \sqrt{(\pi/2)}r_a/\omega_b$, where r_a [m] is the receiver aperture radius, ω_b is the beamwaist, and $A_0 = \mathrm{erf}(\nu)^2$. Finally, defining θ_d as the deviation angle, the conditional probability for the PDF of h_{pl} can be found as

$$f_{pl|\theta_d}(h_{pl}) = \frac{\eta_s^2}{2\pi q_H} \int_{-\pi}^{\pi} \frac{h_{pl}^{\eta_s^2\xi(\varphi)-1}}{(A_0\cos\theta_d)^{\eta_s^2\xi(\varphi)}} d\varphi. \quad (4)$$

AOA Fluctuations: can be divided into two parts *i.e.*, (*i*) UAV movement- and (*ii*) turbulence-induced. The latter is the result of refractive index variations due to atmospheric turbulence. The AOA fluctuations refer to the random variations in the direction from which an optical beam arrives at a receiver due to atmospheric turbulence. The impact of UAV movement on the received intensity that can be subject of future investigation is not included in this work. Assuming that the Gaussian distributed random variable (RV) θ_d is Rayleigh distributed, the PDF of θ_d is given by [31]

$$f_{\theta_d}(\theta_d) = \frac{\theta_d}{\sigma_0^2}\exp\left(-\frac{\theta_d^2}{2\sigma_0^2}\right), \quad \theta_d \geq 0, \quad (5)$$

where σ_0^2 is the variance of θ_d.

IV. Signal Model

This section distinguishes two UAVs-assisted FSO connectivity paths linking GS1 to GS2. Specifically, the first path consists of UAV1, while the second one involves both UAV1 and UAV2. We call such paths as (*i*) RIS-embedded one-UAV FSO and (*ii*) RIS-embedded two-UAVs FSO path, respectively. Specifically, we assume UAV1 (UAV2) is equipped with an $N(M)$-reflecting elements RIS, with $N(M) \in \mathbf{Z}^+$.

A. RIS-embedded one-UAV FSO Path

With reference to Fig. 1, for the path with UAV1 acting as relay node, GS1 transmits a signal to UAV1, which redirects to GS2. The received signal at GS2 can be written as

$$y = \sum_{n=1}^{N} h_n \beta_n e^{j\theta_n} g_n x + n_0, \quad (6)$$

where $h_n = L_1^{-\rho/2} v_n e^{-j\phi_n}$ and $g_n = L_2^{-\rho/2} u_n e^{-j\varphi_n}$ are the gains of first-link (*i.e.*, from GS1 to the n-th RIS element in UAV1) and second-link (*i.e.*, from the n-th RIS element in UAV1 to GS2) channels, with $n = \{1,\ldots,N\}$. In Eq. (6), ρ is the path-loss index, L_1 [m] and L_2 [m] are the distances for the GS1-UAV1 and UAV1-GS2, respectively. It follows that ϕ_n and φ_n are the phase shifts of the transmitted signal x along the first and second link, with reference to the n-th reflecting element of UAV1, respectively. Also, $\beta_n \in [0,1]$ is the n-th reflection amplitude, $\theta_n \in [0, 2\pi]$ is the n-th phase shift induced by the reflecting meta-surface.

Arranging Eq. (6), and to provide the maximum SNR, we set $\theta_n = \phi_n + \varphi_n$, thus obtaining

$$y = (L_1 L_2)^{-\rho/2} \sum_{n=1}^{N} v_n \beta_n u_n x + n_0. \quad (7)$$

Then, the instantaneous electrical SNR will be

$$\gamma = \left(\sum_{n=1}^{N} v_n \beta_n u_n\right)^2 P_t^2 / \left[(L_1 L_2)^{\rho}\,\sigma_n^2\right], \quad (8)$$

where P_t [W] is the transmitted electrical power and σ_n^2 is the variance of the additive white Gaussian noise (AWGN).

If we select the reflection amplitude β_n for each reflecting element equal as $\beta_n = \mathcal{B}$, then the instantaneous electrical SNR can be written as

$$\gamma = \left(\sum_{i=1}^{N} \mathcal{H}_{1i}\right)^2 \mathcal{B}^2 \overline{\gamma}, \quad (9)$$

with $\mathcal{H}_{1i} = v_n u_n$ denoting the total channel state for the first path, as indicated by the subscript 1, and $\overline{\gamma}$ as the average SNR expressed as $\overline{\gamma} = P_t^2/(L_1 L_2)^{\rho}\,\sigma_n^2$. Notice that according to [32], the sum of $\mathcal{F}$-RVs can be represented by an $\mathcal{F}$-RV. Assuming that RVs $\mathcal{H}_{11}, \mathcal{H}_{12}, \ldots, \mathcal{H}_{1N}$ are independent and identically distributed (i.i.d.) then $\mathcal{H}_{11} = \mathcal{H}_{12} = \ldots = \mathcal{H}_{1N} = \mathcal{H}_1$ and the sum of these RV can be written as

$$\mathcal{H}_{1\mathcal{F}} = \sum_{i=1}^{N} \mathcal{H}_{1i} = N\mathcal{H}_1, \quad (10)$$

where the parameters a and b given in Eq. (2) change respectively to

$$a_{\mathcal{F}} = \frac{-2(H_{\mathcal{F}} - Y_{\mathcal{F}})}{H_{\mathcal{F}} - 2Y_{\mathcal{F}} + H_{\mathcal{F}}Y_{\mathcal{F}}}, \quad b_{\mathcal{F}} = \frac{4H_{\mathcal{F}} - 3Y_{\mathcal{F}} - 1}{2H_{\mathcal{F}} - Y_{\mathcal{F}} - 1}, \quad (11)$$

$$H_{\mathcal{F}} \triangleq (H - \varepsilon - 1)/N + 1, \quad (12)$$

$$\begin{aligned} Y_{\mathcal{F}} \triangleq \Big[&(H-\varepsilon)Y + N^2 + 3N(H-\varepsilon) - 3N \\ &- 3(H-\varepsilon) + 2\Big] / \Big[N(H-\varepsilon) - N + N^2\Big], \end{aligned} \quad (13)$$

$$H = \frac{(1+a)(b-1)}{a(b-2)}, \text{ and } Y = \frac{(b-1)(2+a)}{a(b-3)}, \quad (14)$$

and ε is the factor that can be adjusted to minimize the difference between the approximate and the exact statistics.

It follows that the expression of SNR in Eq. (9) becomes:

$$\gamma = \overline{\gamma} N^2 \mathcal{B}^2 \mathcal{H}_1^2. \quad (15)$$

B. RIS-embedded two-UAVs FSO Path

With reference to Fig. 1, for the path comprised to two UAVs, GS1 transmits a signal to UAV1, which redirects to UAV2, and then to GS2. The received signal at GS2 can be written as

$$y = \left(\sum_{n=1}^{N} h_n \beta_n e^{j\theta_n} g_n \sum_{m=1}^{M} s_{mn} \beta_m e^{j\zeta_m} \right) x + n_0, \quad (16)$$

where $h_n = L_1^{-\rho/2} v_n e^{-j\phi_n}$, $g_n = L_2^{-\rho/2} u_n e^{-j\varphi_n}$ and $s_{m,n} = L_3^{-\rho/2} r_{m,n} e^{-j\psi_{m,n}}$ are the gains of the first-link (*i.e.*, from GS1 to UAV1), second-link (*i.e.*, from UAV1 to UAV2), and third-link (*i.e.*, from UAV2 to GS2) channel, respectively, with $n(m) = \{1, \ldots, N(M)\}$. Similarly to what has been done for the case of one-UAV FSO path, we set the following condition *i.e.*, $\theta_n + \zeta_m = \phi_n + \varphi_n + \psi_n$, to provide the maximum SNR. We then obtain:

$$y = (L_1 L_2 L_3)^{-\rho/2} \times \sum_{m=1}^{M} \left(\sum_{n=1}^{N} v_n u_n r_{mn} \beta_n \beta_m \right) x + n_0, \quad (17)$$

and the instantaneous electrical SNR will be

$$\gamma = \left[\sum_{m=1}^{M} \left(\sum_{n=1}^{N} v_n u_n r_{mn} \beta_n \beta_m \right) \right]^2 \frac{P_t^2}{(L_1 L_2 L_3)^{\rho} \sigma_n^2}. \quad (18)$$

Furthermore, if we select the reflection amplitudes β_n and β_m for each reflecting element equal as $\beta_n = \beta_m = \mathcal{B}$ then, the instantaneous electrical SNR becomes

$$\gamma = \left[\sum_{m=1}^{M} \sum_{n=1}^{N} \mathcal{H}_{2,mn} \right]^2 \mathcal{B}^4 \overline{\gamma}, \quad (19)$$

where $\overline{\gamma} = P_t^2 / \left((L_1 L_2 L_3)^{\rho} \sigma_n^2 \right)$ is the average SNR, and $\mathcal{H}_{2,mn} = v_n u_n r_{mn}$ denotes the channel state related to the m^{th} and n^{th} RIS element for the second UAV path, as indicated by the subscript 2. Similar to the case of one-UAV path, we assume that RVs $\mathcal{H}_{2,11}, \mathcal{H}_{2,12}, \ldots, \mathcal{H}_{2,MN}$ are i.i.d., and then $\mathcal{H}_{2,11} = \mathcal{H}_{2,12} = \ldots = \mathcal{H}_{2,MN} = \mathcal{H}_2$. It follows that the sum of these RVs can be written as

$$\mathcal{H}_{2\mathcal{F}} = \sum_{m=1}^{M} \sum_{n=1}^{N} \mathcal{H}_{2,mn} = MN\mathcal{H}_2, \quad (20)$$

where the parameters a and b are as in Eq. (11). However, in this case $H_{\mathcal{F}}$ and $Y_{\mathcal{F}}$ become respectively as

$$H_{\mathcal{F}} \triangleq (H - \varepsilon - 1)/(MN) + 1, \quad (21)$$

$$Y_{\mathcal{F}} \triangleq \left[(H - \varepsilon)(Y + 3MN - 3) + (MN)^2 - 3MN + 2 \right] / \left[MN(H - \varepsilon) - MN + (MN)^2 \right]. \quad (22)$$

It follows then the SNR in Eq. (19) can be expressed as:

$$\gamma = \overline{\gamma} (MN)^2 \mathcal{B}^4 \mathcal{H}_2^2. \quad (23)$$

Although this study focuses on the analysis of RIS-mounted two-UAVs FSO communication link, the mathematical framework can be extended for any number of UAVs. Assuming $\mathcal{K}$ UAVs, each mounted with the number of $\mathcal{N}_1, \mathcal{N}_2 \ldots \mathcal{N}_{\mathcal{K}} \in \mathbf{Z}^+$ RIS elements, for maximum SNR the received signal and the instantaneous electrical SNR can be written respectively by

$$y = n_0 + (L_1 L_2 \ldots L_{\mathcal{K}+1})^{-\rho/2} \sum_{m_{\mathcal{K}}=1}^{\mathcal{N}_{\mathcal{K}}} \sum_{m_{\mathcal{K}-1}=1}^{\mathcal{N}_{\mathcal{K}-1}} \ldots \times \left(\sum_{m_1=1}^{\mathcal{N}_1} v_{m_1} u_{m_1} r_{m_{\mathcal{K}} \ldots m_1} \beta_{m_1} \ldots \beta_{m_{\mathcal{K}}} \right) x, \quad (24)$$

$$\gamma = \frac{P_t^2}{(L_1 L_2 \ldots L_{\mathcal{K}+1})^{\rho} \sigma_n^2} \left[\sum_{m_{\mathcal{K}}=1}^{\mathcal{N}_{\mathcal{K}}} \sum_{m_{\mathcal{K}-1}=1}^{\mathcal{N}_{\mathcal{K}-1}} \ldots \times \left(\sum_{m_1=1}^{\mathcal{N}_1} v_{m_1} u_{m_1} r_{m_{\mathcal{K}} \ldots m_1} \beta_{m_1} \ldots \beta_{m_{\mathcal{K}}} \right) \right]^2. \quad (25)$$

Given that each reflecting element has equal reflection coefficient as $\beta_{m_1} = \ldots = \beta_{m_{\mathcal{K}}} = \mathcal{B}$ and the average SNR is $\overline{\gamma} = P_t^2 / \left[(L_1 L_2 \ldots L_{\mathcal{K}+1})^{\rho} \sigma_n^2 \right]$, the instantaneous electrical SNR will be obtained as

$$\gamma = \left[\sum_{m_1=1}^{\mathcal{N}_1} \sum_{m_2=1}^{\mathcal{N}_2} \ldots \sum_{m_{\mathcal{K}}=1}^{\mathcal{N}_{\mathcal{K}}} \mathcal{H}_{\mathcal{K},m_1 \ldots m_{\mathcal{K}}} \right]^2 \mathcal{B}^{2\mathcal{K}} \overline{\gamma}. \quad (26)$$

Assuming that the RVs $\mathcal{H}_{\mathcal{K},1\ldots1}, \mathcal{H}_{\mathcal{K},1\ldots2}, \ldots, \mathcal{H}_{\mathcal{K},\mathcal{N}_1\ldots\mathcal{N}_{\mathcal{K}}}$ are i.i.d., and then $\mathcal{H}_{\mathcal{K},1\ldots1}, \mathcal{H}_{\mathcal{K},1\ldots2}, \ldots, \mathcal{H}_{\mathcal{K},\mathcal{N}_1\ldots\mathcal{N}_{\mathcal{K}}} = \mathcal{H}_{\mathcal{K}}$, the channel state can be written as the sum of these RVs *i.e.,*

$$\mathcal{H}_{\mathcal{K}\mathcal{F}} = \sum_{m_1=1}^{\mathcal{N}_1} \ldots \sum_{m_{\mathcal{K}}=1}^{\mathcal{N}_{\mathcal{K}}} \mathcal{H}_{\mathcal{K},m_1..m_{\mathcal{K}}} = (\mathcal{N}_1 \ldots \mathcal{N}_{\mathcal{K}}) \mathcal{H}_{\mathcal{K}}, \quad (27)$$

where the $\mathcal{F}$-turbulence parameters a and b can be found by Eqs. (11), (12) and (13) and replacing N with the multiplication $\mathcal{N}_1 \mathcal{N}_2 \ldots \mathcal{N}_{\mathcal{K}}$. Then, the instantaneous SNR will be as

$$\gamma = \overline{\gamma} (\mathcal{N}_1 \mathcal{N}_2 \ldots \mathcal{N}_{\mathcal{K}})^2 \mathcal{B}^{2\mathcal{K}} \mathcal{H}_{\mathcal{K}}^2. \quad (28)$$

V. Channel PDF Analysis

Combining the effects of the attenuation loss h_{al}, atmospheric turbulence h_{at}, pointing error h_{pl}, and AOA fluctuations h_{af}, the channel state for ground-to-ground through UAV communication link can be modeled by

$$h = h_{al} h_{at} h_{pl} h_{af}. \quad (29)$$

As also assumed in [31], posing $h_{ag} = h_{al} h_{at} h_{pl}$, we consider the channel states for attenuation loss, atmospheric turbulence, and pointing error are conditioned on θ_d according to the following relationship, using $\Delta_x = \frac{h_{ag}}{A_0 h_{al} \cos\theta_d}$, *i.e.*

$$f_{h_{ag}|\theta_d}(h_{ag}) = \int_{\Delta_x}^{\infty} \frac{f_{h_{pl}|\theta_d}\left(\frac{h_{ag}}{h_{al} h_{at}} \right)}{h_{al} h_{at}} f_{h_{at}}(h_{at}) dh_{at}. \quad (30)$$

Inserting Eq. (4) and (1) into Eq. (30), we obtain

$$f_{h_{ag}|\theta_d}(h_{ag}) = \frac{\eta_s^2 a^a (b-1)^{-a}}{2\pi q_H \mathfrak{B}(a,b)} \int_{\Delta_x}^{\infty} \frac{h_{at}^{a-\eta_s^2\xi(\varphi)-1} dh_{at}}{\left(1 + \frac{a}{b-1} h_{at}\right)^{a+b}} \times \int_{-\pi}^{\pi} \frac{h_{ag}^{\eta_s^2\xi(\varphi)-1}}{(A_0 h_{al} \cos\theta_d)^{\eta_s^2\xi(\varphi)}} d\varphi. \quad (31)$$

We can solve h_{at} dependent integral in Eq. (31) according to Eq. (3.194-2) given in [33], and we get

$$f_{h_{ag}}|\theta_d(h_{ag}) = \frac{\eta_s^2 \left(A_0 h_{al}\cos\theta_d\right)^b h_{ag}^{-(b+1)}}{2\pi q_H \mathfrak{B}(a,b) a^b (b-1)^{-b}} \times \int_{-\pi}^{\pi} \frac{d\varphi}{b+\eta_s^2\xi(\varphi)}\, {}_2F_1\left(\begin{matrix} a+b, b+\eta_s^2\xi(\varphi); \\ b+\eta_s^2\xi(\varphi)+1; \end{matrix} -\frac{1}{\left(\frac{a}{b-1}\right)\left(\frac{h_{ag}}{A_0 h_{al}\cos\theta_d}\right)}\right), \tag{32}$$

where ${}_2F_1(\cdot)$ is the Hypergeometric function, which can be further expanded by using Eq. 17 in [34]. Furthermore, since we can express $\Gamma(x) = (x-1)!$, Eq. (32) finally becomes

$$fh_{ag|\theta_d}(h_{ag}) = \frac{\eta_s^2 (A_0 h_{al}\cos\theta_d)^b h_{ag}^{-1-b}}{2\pi q_H \Gamma(a)\Gamma(b) a^b (b-1)^{-b}} \int_{-\pi}^{\pi} d\varphi \times G_{2,2}^{2,1}\left(\frac{a h_{ag}}{(b-1)A_0 h_{al}\cos\theta_d}\middle| \begin{matrix} 1, b+\eta_s^2\xi(\varphi)+1 \\ a+b, b+\eta_s^2\xi(\varphi) \end{matrix}\right). \tag{33}$$

The PDF of the channel state in Eq. (29) can be found as

$$f_h(h) = \int_0^{\theta_{FOV}} f_{h_{ag|\theta_d}}(h) f_{\theta_d}(\theta_d) d\theta_d + \delta(h) \int_{\theta_{FOV}}^{\infty} f_{\theta_d}(\theta_d) d\theta_d, \tag{34}$$

and through the calculations shown in Appendix A, it becomes

$$f_h(h) = \frac{\eta_s^2 (b-1)^b \left[1-\exp\left(-\frac{\theta_{FOV}^2}{2\sigma_0^2}\right)\right]}{2\pi q_H \Gamma(a)\Gamma(b) a^b (A_0 h_{al})^{-b}} \int_{-\pi}^{\pi} h^{-b-1} d\varphi \times G_{2,2}^{2,1}\left(\frac{a}{(b-1)A_0 h_{al}} h \middle| \begin{matrix} 1, b+\eta_s^2\xi(\varphi)+1 \\ a+b, b+\eta_s^2\xi(\varphi) \end{matrix}\right) + \delta(h)\exp\left(-\theta_{FOV}^2/(2\sigma_0^2)\right). \tag{35}$$

VI. RIS-embedded one-UAV FSO Path

A. Outage Probability Derivation

Using the SNR definition given in Eq. (15), the SNR dependent PDF of the channel will be $\mathcal{H}_1 = \sqrt{\gamma}/(\sqrt{\overline{\gamma}}N\mathcal{B})$, from which we can obtain $f_\gamma(\gamma) = f_{\mathcal{H}_1}\left[\sqrt{\gamma}/(\sqrt{\overline{\gamma}}N\mathcal{B})\right]|d\mathcal{H}_1/d\gamma|$. Then, we have

$$f_\gamma(\gamma) = \frac{\eta_s^2 (b-1)^b \left[1-\exp\left(-\frac{\theta_{FOV}^2}{2\sigma_0^2}\right)\right]}{2\pi q_H \Gamma(a)\Gamma(b) a^b (A_0 h_{al})^{-b}} \int_{-\pi}^{\pi} d\varphi \times \frac{\gamma^{-b/2-1}}{2\left(N\mathcal{B}\right)^{-b}\overline{\gamma}^{-b/2}} \times G_{2,2}^{2,1}\left(\frac{a(b-1)^{-1}\sqrt{\gamma}}{A_0 h_{al}\sqrt{\overline{\gamma}}N\mathcal{B}}\middle| \begin{matrix} 1, b+\eta_s^2\xi(\varphi)+1 \\ a+b, b+\eta_s^2\xi(\varphi) \end{matrix}\right) + \frac{1}{2N\mathcal{B}\sqrt{\overline{\gamma}\gamma}}\delta\left(\frac{\sqrt{\gamma}}{\sqrt{\overline{\gamma}}N\mathcal{B}}\right)\exp\left(-\frac{\theta_{FOV}^2}{2\sigma_0^2}\right). \tag{36}$$

Through some calculations detailed in Appendix B, we can derive the outage probability, defined as the probability of the instantaneous SNR γ falls below the defined threshold SNR level γ_{th}, *i.e.*

$$P_{out} = \Pr(\gamma \le \gamma_{th}) = F_\gamma(\gamma_{th}), \tag{37}$$

which becomes as in Eq. (B.3). Using Eq. (07.34.16.0001.01) of [35], Eq. (B.3) simplifies to

$$Pout = \frac{\eta_s^2\left[1-\exp\left(-\frac{\theta_{FOV}^2}{2\sigma_0^2}\right)\right]}{2\pi q_H \Gamma(a)\Gamma(b)} \int_{-\pi}^{\pi} d\varphi \times G_{3,3}^{2,2}\left(\frac{a\sqrt{\gamma_{th}/\overline{\gamma}}}{(b-1)A_0 h_{al} N\mathcal{B}}\middle| \begin{matrix} 1-b, 1, \eta_s^2\xi(\varphi)+1 \\ a, \eta_s^2\xi(\varphi), 0 \end{matrix}\right) + \exp\left(-\theta_{FOV}^2/(2\sigma_0^2)\right). \tag{38}$$

B. Average BER Derivation

Assuming the error probability of an intensity modulation/direct detection (IM/DD) on-off keying (OOK) system, with equiprobable bits "1" and "0" so that $p(e|1) = p(e|0)$, then the conditioned probability will result as $P_b(e|\gamma) = \mathcal{Q}\left(\sqrt{\gamma/2}\right) = \frac{1}{2}\operatorname{erfc}\left(\frac{\sqrt{\gamma}}{2}\right)$, where $\mathcal{Q}\left(\sqrt{2}x\right) = \frac{1}{2}\operatorname{erfc}(x)$. Then, the error probability becomes:

$$< BER >= P_b(e) = \int_0^{\infty} P_b(e|\gamma) f_\gamma(\gamma) d\gamma. \tag{39}$$

Inserting the PDF of the SNR given in Eq. (36) and the expression of $P_b(e|\gamma)$ into Eq. (39), we obtain

$$P_b(e) = \frac{\eta_s^2 (b-1)^b \left[1-\exp\left(-\frac{\theta_{FOV}^2}{2\sigma_0^2}\right)\right]}{8\pi q_H \Gamma(a)\Gamma(b) a^b \left(A_0 h_{al} N\mathcal{B}\right)^{-b}\overline{\gamma}^{-b/2}} \int_{-\pi}^{\pi} d\varphi \times \int_0^{\infty} \gamma^{-b/2-1}\operatorname{erfc}\left(\frac{\sqrt{\gamma}}{2}\right) d\gamma \times G_{2,2}^{2,1}\left(\frac{a(b-1)^{-1}\sqrt{\gamma}}{A_0 h_{al}\sqrt{\overline{\gamma}}N\mathcal{B}}\middle| \begin{matrix} 1, b+\eta_s^2\xi(\varphi)+1 \\ a+b, b+\eta_s^2\xi(\varphi) \end{matrix}\right) + \frac{1}{2}\exp\left(-\frac{\theta_{FOV}^2}{2\sigma_0^2}\right)\frac{1}{2N\mathcal{B}\sqrt{\overline{\gamma}}} \times \int_0^{\infty} \frac{1}{\sqrt{\gamma}}\operatorname{erfc}\left(\frac{\sqrt{\gamma}}{2}\right)\delta\left(\frac{\sqrt{\gamma}}{\sqrt{\overline{\gamma}}N\mathcal{B}}\right) d\gamma. \tag{40}$$

According to the calculations detailed in Appendix C, we can finally derive the error probability *i.e.*,

$$P_b(e) = \frac{2^{a+b-1}\eta_s^2\left[1-\exp\left(-\frac{\theta_{FOV}^2}{2\sigma_0^2}\right)\right]}{16\pi^2\sqrt{\pi}q_H\Gamma(a)\Gamma(b)} \int_{-\pi}^{\pi} d\varphi \times G_{6,5}^{4,4}\left(\frac{4a^2(b-1)^{-2}}{\left(A_0 h_{al}\sqrt{\overline{\gamma}}N\mathcal{B}\right)^2}\middle| \begin{matrix} \Delta_{1,1}, .., \Delta_{1,6} \\ \Delta_{2,1}, .., \Delta_{2,5} \end{matrix}\right) + 0.5\exp\left(-\theta_{FOV}^2/(2\sigma_0^2)\right), \tag{41}$$

where $\Delta_{1,1}, \ldots, \Delta_{1,6} = \frac{1-b}{2}, \frac{2-b}{2}, 1, \frac{1}{2}, \frac{\eta_s^2\xi(\varphi)+1}{2}, \frac{\eta_s^2\xi(\varphi)+2}{2}$, and $\Delta_{2,1}, \ldots, \Delta_{2,5} = \frac{a}{2}, \frac{a+1}{2}, \frac{\eta_s^2\xi(\varphi)}{2}, \frac{\eta_s^2\xi(\varphi)+1}{2}, 0$.

VII. RIS-embedded two-UAVs FSO Path

Using the SNR definition given in Eq. (23), the SNR dependent PDF of the channel can be expressed as

$$\mathcal{H}_2 = \sqrt{\gamma}/\left(\sqrt{\overline{\gamma}}MN\mathcal{B}^2\right), \tag{42}$$

from which we have $f_\gamma(\gamma) = f_{\mathcal{H}_2}\left[\frac{\sqrt{\gamma}}{\sqrt{\overline{\gamma}}MN\mathcal{B}^2}\right]\left|\frac{d\mathcal{H}_2}{d\gamma}\right|$. Then, using the PDF in Eq. (35), we obtain

$$\begin{aligned} f_\gamma(\gamma) &= \frac{\eta_s^2\,(b-1)^b\left[1-\exp\left(-\frac{\theta_{FOV}^2}{2\sigma_0^2}\right)\right]\gamma^{-\frac{b}{2}-1}}{4\pi q_H\Gamma(a)\Gamma(b)a^b(A_0h_{al}\sqrt{\overline{\gamma}}MN\mathcal{B}^2)^{-b}} \\ &\times\int_{-\pi}^{\pi} G_{2,2}^{2,1}\left[\frac{a(b-1)^{-1}\sqrt{\gamma}}{A_0h_{al}\sqrt{\overline{\gamma}}MN\mathcal{B}^2}\middle|\begin{matrix}1, b+\eta_s^2\xi(\varphi)+1\\ a+b, b+\eta_s^2\xi(\varphi)\end{matrix}\right]d\varphi \\ &+\frac{\exp\left(-\frac{\theta_{FOV}^2}{2\sigma_0^2}\right)}{2\sqrt{\overline{\gamma}}MN\mathcal{B}^2\sqrt{\gamma}}\delta\left(\frac{\sqrt{\gamma}}{\sqrt{\overline{\gamma}}MN\mathcal{B}^2}\right). \end{aligned} \tag{43}$$

A. Outage Probability Derivation

From Eq. (43), through some calculations detailed in Appendix D, we can obtain cumulative distribution function (CDF) of the channel as in Eq. (D.2). Then, using Eq. (37) and applying Eq. (07.34.16.0001.01) of [35], we can finally derive the outage probability as

$$\begin{aligned} P_{out} &= \frac{\eta_s^2\left[1-\exp\left(-\frac{\theta_{FOV}^2}{2\sigma_0^2}\right)\right]}{2\pi q_H\Gamma(a)\Gamma(b)}\int_{-\pi}^{\pi}d\varphi \\ &\times G_{3,3}^{2,2}\left(\frac{a\,(b-1)^{-1}\sqrt{\gamma_{th}}}{A_0h_{al}\sqrt{\overline{\gamma}}MN\mathcal{B}^2}\middle|\begin{matrix}1-b, 1, \eta_s^2\xi(\varphi)+1\\ a, \eta_s^2\xi(\varphi), 0\end{matrix}\right) \\ &+\exp\left(-\theta_{FOV}^2/(2\sigma_0^2)\right). \end{aligned} \tag{44}$$

B. Average BER Derivation

We provide all the calculations needed to derive the average BER for the two-UAVs assisted FSO path in Appendix E. Eq. (E.2) represents the average BER for a two-UAV path, which is expressed as:

$$\begin{aligned} P_b(e) &= \frac{2^{a+b-1}\eta_s^2\left[1-\exp\left(-\frac{\theta_{FOV}^2}{2\sigma_0^2}\right)\right]}{16\pi^2\sqrt{\pi}q_H\Gamma(a)\Gamma(b)}\int_{-\pi}^{\pi}d\varphi \\ &\times G_{6,5}^{4,4}\left(\frac{4a^2(b-1)^{-2}}{\left(A_0h_{al}\sqrt{\overline{\gamma}}MN\mathcal{B}\right)^2}\middle|\begin{matrix}\Delta_{1,1},..,\Delta_{1,6}\\ \Delta_{2,1},..,\Delta_{2,5}\end{matrix}\right) \\ &+0.5\exp\left(-\theta_{FOV}^2/(2\sigma_0^2)\right). \end{aligned} \tag{45}$$

It should be noted that the average BER, as well as the outage probability for multiple UAV scenarios, can be derived from the expression of the instantaneous SNR given in Eq. (28).

VIII. Asymptotic Analysis

A. High SNR Regime

Asymptotic analysis at high SNR level offers a computationally tractable approach to understanding the fundamental performance limits of optical wireless communication (OWC) systems. By focusing on dominant terms on the performance and simplifying complex mathematical models, this analysis provides valuable insights into system behavior, guiding the optimization of system parameters and design strategies. Furthermore, they facilitate comparisons with theoretical bounds that give perspective to researchers in evaluating the effectiveness and efficiency of the FSO communication schemes. Leveraging on above considerations, this section presents the asymptotic analysis of both outage probability and average BER in high SNR regime.

1) Outage Probability: According to [36], the asymptotic expansion of H-function under specific conditions can be expressed by

$$H_{p,q}^{m,n}\left(z\middle|\begin{matrix}(a_i,\alpha_i)_{1,p}\\ (b_i,\beta_i)_{1,q}\end{matrix}\right) = \sum_{j=1}^{m}h_jz^{\frac{b_j}{\beta_j}}, \quad z\to 0 \tag{46}$$

where

$$h_j = \frac{\prod\limits_{\substack{i=1\\ i\neq j}}^{m}\Gamma\left(b_i-\frac{b_j\beta_i}{\beta_j}\right)\prod\limits_{i=1}^{n}\Gamma\left(1-a_i+\frac{b_j\alpha_i}{\beta_j}\right)}{\beta_j\prod\limits_{\substack{i=\\ n+1}}^{p}\Gamma\left(a_i-\frac{b_j\alpha_i}{\beta_j}\right)\prod\limits_{\substack{i=\\ m+1}}^{q}\Gamma\left(1-b_i+\frac{b_j\beta_i}{\beta_j}\right)}, \tag{47}$$

and $j = 1,\ldots,m$. Using the relationship between Meijer-G and H-functions, and applying Eqs. (46) and (47) to Eqs. (38) and (44) respectively, the outage probabilities for both one UAV and two UAVs FSO paths can be expressed by

$$\begin{aligned} P_{out_{\overline{\gamma}\gg 1}} &= \frac{\eta_s^2\left[1-\exp\left(-\frac{\theta_{FOV}^2}{2\sigma_0^2}\right)\right]}{2\pi q_H\Gamma(a)\Gamma(b)}\int_{-\pi}^{\pi}\sum_{j=1}^{2}\Upsilon_j\overline{\gamma}^{-\Theta_j}d\varphi \\ &+\exp\left(-\theta_{FOV}^2/(2\sigma_0^2)\right), \end{aligned} \tag{48}$$

where

$$\Upsilon_1 = \frac{\Gamma(a+b)}{a(\eta_s^2\xi(\varphi)-a)}\left[\frac{a\sqrt{\gamma_{th}}}{(b-1)A_0h_{al}N\mathcal{B}\Delta_1}\right]^a, \tag{49}$$

$$\begin{aligned} \Upsilon_2 &= \frac{\Gamma(a-\eta_s^2\xi(\varphi))\Gamma(b+\eta_s^2\xi(\varphi))}{\eta_s^2\xi(\varphi)} \\ &\times\left[\frac{a\sqrt{\gamma_{th}}}{(b-1)A_0h_{al}N\mathcal{B}\Delta_1}\right]^{\eta_s^2\xi(\varphi)}, \end{aligned} \tag{50}$$

with $\Theta_1 = a/2$, $\Theta_2 = \eta_s^2\xi(\varphi)/2$, $\Delta_1 = 1$ for one UAV FSO path, and $\Delta_1 = M\mathcal{B}$ for two UAV FSO path, respectively.

2) Average BER: Using the procedures given in Eqs. (46) and (47) above, the average BER of both one UAV and two UAVs FSO paths given in Eqs. (41) and (45) respectively can be approximated in high SNR regime as

$$\begin{aligned} P_b(e)_{\overline{\gamma}\gg 1} &= \frac{2^{a+b-1}\eta_s^2\left[1-\exp\left(-\frac{\theta_{FOV}^2}{2\sigma_0^2}\right)\right]}{32\pi^2\sqrt{\pi}q_H\Gamma(a)\Gamma(b)} \\ &\times\int_{-\pi}^{\pi}\sum_{j=1}^{3}\Xi_j\overline{\gamma}^{-\Psi_j}d\varphi+\frac{1}{2}\exp\left(-\frac{\theta_{FOV}^2}{2\sigma_0^2}\right), \end{aligned} \tag{51}$$

where

$$\Psi_j = \left\{\frac{a}{2}, \frac{a+1}{2}, \frac{\eta_s^2\xi(\varphi)}{2}\right\}, \tag{52}$$

$$\Xi_1 = \frac{8\Gamma(0.5)\Gamma\left(\frac{a+b+1}{2}\right)\Gamma\left(\frac{a+b}{2}\right)\Gamma\left(\frac{a+1}{2}\right)}{a(\eta_s^2\xi(\varphi)-a)} \times \left[\frac{2a}{(b-1)A_0 h_{al} N\mathcal{B}\Delta_1}\right]^a, \tag{53}$$

$$\Xi_2 = \frac{8\Gamma(-0.5)\Gamma\left(\frac{a+b+2}{2}\right)\Gamma\left(\frac{a+b+1}{2}\right)\Gamma\left(\frac{a+2}{2}\right)}{(a+1)(\eta_s^2\xi(\varphi)-a-1)} \times \left[\frac{2a}{(b-1)A_0 h_{al} N\mathcal{B}\Delta_1}\right]^{a+1}, \tag{54}$$

$$\Xi_3 = \frac{4\Gamma\left(\frac{a-\eta_s^2\xi(\varphi)}{2}\right)\Gamma\left(\frac{a-\eta_s^2\xi(\varphi)+1}{2}\right)\Gamma\left(\frac{b+\eta_s^2\xi(\varphi)+1}{2}\right)}{\eta_s^2\xi(\varphi)} \times \Gamma\left(\frac{b+\eta_s^2\xi(\varphi)}{2}\right)\Gamma\left(\frac{\eta_s^2\xi(\varphi)+1}{2}\right) \times \left[\frac{2a}{(b-1)A_0 h_{al} N\mathcal{B}\Delta_1}\right]^{\eta_s^2\xi(\varphi)}. \tag{55}$$

B. Large Number of RIS Elements

To give more design insights, the asymptotic analysis when the number of reflecting elements approaches infinity should be considered. Taking into account the performance trends as the number of RIS elements tends towards infinity, the asymptotic approach will provide researchers invaluable insights into the fundamental limits and optimization strategies for FSO systems. To do this, the asymptotic analysis for large number of RIS elements is given in this section.

1) Outage Probability: Following the procedures given in Eqs. (46) and (47), the outage probability of RIS-aided one- and two-UAV FSO communication system can be generalized and expressed for Eqs. (38) and (44) as

$$P_{out_{M\times N\gg 1}} = \frac{\eta_s^2\left[1-\exp\left(-\frac{\theta_{FOV}^2}{2\sigma_0^2}\right)\right]}{2\pi q_H\Gamma(a)\Gamma(b)} \int_{-\pi}^{\pi} d\varphi \times \sum_{j=1}^{2} \aleph_j (N\Delta_2)^{-\Theta_j} + \exp\left(-\frac{\theta_{FOV}^2}{2\sigma_0^2}\right), \tag{56}$$

where $\aleph_{1,2} = \Upsilon_{1,2}\left[N\Delta_1/\left(\sqrt{\bar{\gamma}}\mathcal{B}\right)\right]^{\Theta_{1,2}}$, with $\Theta_1 = a$, $\Theta_2 = \eta_s^2\xi(\varphi)$, $\Delta_2 = 1$ for one UAV FSO path, and $\Delta_2 = M$ for two UAVs FSO path, respectively.

2) Average BER: Again, using Eqs. (46) and (47), the average BER of RIS-aided one- and two-UAVs FSO links given in Eqs. (41) and (45) can be approximated as

$$P_b(e)_{M\times N\gg 1} = \frac{2^{a+b-1}\eta_s^2\left[1-\exp\left(-\frac{\theta_{FOV}^2}{2\sigma_0^2}\right)\right]}{32\pi^2\sqrt{\pi}q_H\Gamma(a)\Gamma(b)} \times \int_{-\pi}^{\pi}\sum_{j=1}^{3}\mathfrak{L}_j(N\Delta_3)^{-\Psi_j}d\varphi + \frac{1}{2}\exp\left(-\frac{\theta_{FOV}^2}{2\sigma_0^2}\right), \tag{57}$$

where $\Delta_3 = 1$ for one UAV, and $\Delta_3 = M$ for two UAVs FSO paths $\Psi_j = \{a, a+1, \eta_s^2\xi(\varphi)\}$, and

$$\mathfrak{L}_{1,2,3} = \Xi_{1,2,3}\left[N\Delta_1/\left(\sqrt{\bar{\gamma}}\mathcal{B}\right)\right]^{\Psi_{1,2,3}}. \tag{58}$$

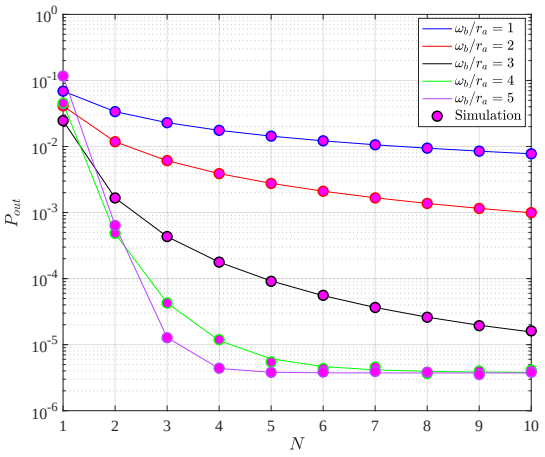

Fig. 2. One-UAV FSO path. Outage probability versus the number of RIS elements for different values of the ratio ω_b/r_a.

IX. Numerical Results

In this section, both average BER and outage probability for the two RIS-based UAVs-assisted FSO connectivity paths are presented depending on various parameters. We provide Monte Carlo simulations with 10^8 realizations to validate the effectiveness and accuracy of the proposed theoretical framework. Finally, we are interested in the behavior of different RIS-embedded paths utilizing the asymptotic approximation in high SNR regime for both average BER and outage probability.

Unless specified in the figures, the simulation parameters are fixed to $\lambda = 1550\,\text{nm}$, $\gamma_{th} = 2\,\text{dB}$, $\bar{\gamma} = 40\,\text{dB}$, $\mathcal{B} = 0.9$, $\zeta_{\text{G1U1}} = 40°$, $\zeta_{\text{U1G2}} = 50°$, $\zeta_{\text{U1U2}} = 75°$, $\zeta_{\text{U2G2}} = 40°$, $h_{\text{UAV1}} = 10\,\text{km}$, $h_{\text{UAV2}} = 5\,\text{km}$, $h_{\text{GS1}} = h_{\text{GS2}} = 10\,\text{m}$, $V = 30\,\text{km}$, $w = 21\,\text{m/s}$, $D_G = 1\,\text{cm}$, $\theta_{FOV} = 60\,\text{mrad}$, $q_H = 0.9$, $\sigma_s = 1 \times r_a$, $\sigma_0 = 12\,\text{mrad}$, and $\omega_b = 1 \times r_a$. Notice that due to Matlab software limitation on the calculation of Meijer G-function, we are showing results for limited RIS elements *i.e.*, $N \leq 6$. It results that increasing the number of RIS elements will enhance significantly the overall performance.

A. Performance of RIS-embedded one-UAV FSO Path

Fig. 2 illustrates the outage probability of one-UAV path versus the number of RIS cells for different values of beam waist. The beam waist ω_b is where optical beam has the narrowest spot size and its intensity is highest along the propagation path [28]. It permits to estimate the beam spreading hence performance degradation due to the atmospheric turbulence effect. The propagating optical beam from the beam waist diverges as it approaches the receiver plane and defines the size of radius of curvature of the beam [37] that shows the beam's susceptibility to refractive index fluctuations resulting from atmospheric turbulence. It is important to choose the beam waist in order to achieve best performance by selecting the optimized initial radius of curvature for Gaussian beam in FSO communication [38]. In Fig. 2, for only one RIS element (*i.e.*, $N = 1$), the increase in beam waist yields a minor improvement in outage performance; however, this trend reverses with the further increase of beam waist. For increasing RIS elements, the increase of beam waist starts

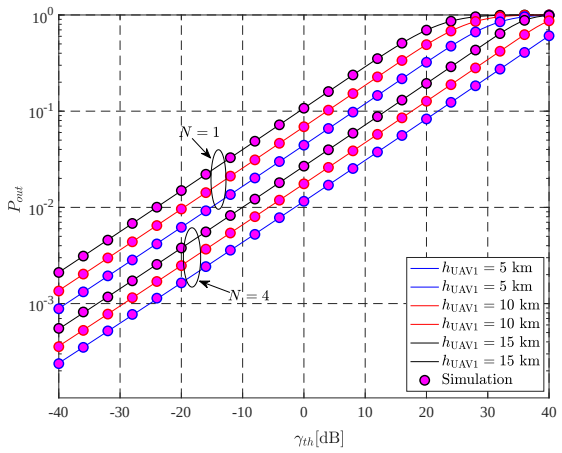

Fig. 3. One-UAV FSO path. Outage probability versus the SNR threshold [dB] in case of different altitudes of UAV1 and number of RIS elements, N.

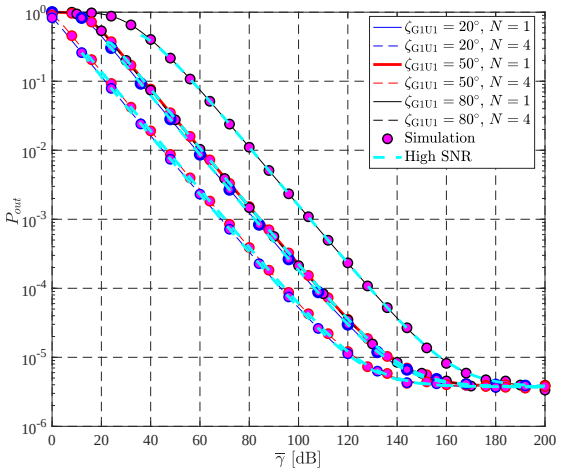

Fig. 4. One-UAV FSO path. Outage probability versus the average SNR [dB] in case of different zenith angles of GS1-UAV path and RIS elements.

to improve the outage performance significantly. This can be physically interpreted as the result of increased probability of optical signal falling on RISs with the increase of beam waist. For example, using $N = 4$ RIS cells (see the green curve in Fig. 2), the outage probability drops from $\sim 1.75 \times 10^{-2}$ to $\sim 4.36 \times 10^{-6}$ when beam waist increases from $\omega_b = r_a$ (blue curve) to $\omega_b = 5r_a$ (magenta curve). It is also seen from Fig. 2 that outage probability maintains its decrease with the increase of number of RISs for small beam waist values; however, the outage probability saturates and almost does not change with the increase of number of RISs when the beam waist takes higher values. This can be noticed for instance in case of $\omega_b = 4r_a$ and $\omega_b = 5r_a$, whose behaviors are almost flat for $N > 6$. We plot the variation of outage performance versus the SNR threshold, for different altitude of UAV and number of RISs in Fig. 3. The monotonic increase of outage probability with the increase of SNR threshold value is observed. It is also seen that keeping the UAV at lower altitude as relay yields better outage performance since a lower altitude corresponds to smaller distances of both GS-UAV uplink and UAV-GS downlink. For example, fixing the SNR threshold value to $\gamma_{th} = 0$ dB and using $N = 1$, the outage probability rises from $\sim 4.4 \times 10^{-2}$ to $\sim 1 \times 10^{-1}$ when the altitude of increases from $h_{\mathrm{UAV1}} = 5$ [km] to $h_{\mathrm{UAV1}} = 15$ [km]. Moreover, the benefit of using RISs on the considered scenario is noticeable through the decrease of outage probability from $\sim 6.9 \times 10^{-2}$ to $\sim 1.7 \times 10^{-2}$ with the increase of number of RIS elements from $N = 1$ to $N = 4$ on setting $\gamma_{th} = 0$ [dB].

The impact of zenith angle, the number of RISs and the average SNR on the outage performance is reflected in Fig. 4. The smaller the zenith angle, the smaller the outage probability and hence the better performance of FSO communication system is observed. For $N = 1$ and $\overline{\gamma} = 100$ [dB], decreasing zenith angle between GS1 and UAV from $\zeta_{\mathrm{G1U1}} = 80°$ to $\zeta_{\mathrm{G1U1}} = 20°$ pulls down the outage probability from $\sim 1.5 \times 10^{-3}$ to $\sim 2.1 \times 10^{-4}$. The undeniable improving effect of higher SNR on the performance of FSO communication system operating both with RIS and without RIS application can also be seen from Fig. 4. An FSO communication between GS1 and GS2 through a UAV having 4 RIS elements operates with the outage performance of $\sim 1.3 \times 10^{-1}$, $\sim 7.1 \times 10^{-3}$, $\sim 6 \times 10^{-5}$ and $\sim 4.2 \times 10^{-6}$ for the average SNR values of $\overline{\gamma} = 20$ [dB], $\overline{\gamma} = 50$ [dB], $\overline{\gamma} = 100$ [dB] and $\overline{\gamma} = 150$ [dB], respectively at zenith angle $\zeta_{\mathrm{G1U1}} = 50°$. We note that relatively very high SNR value (*i.e.*, $\overline{\gamma} = 150$ [dB]) is required to provide the outage probability at level of 10^{-6}. This is because the uplink and downlink movement of the optical signal through a UAV loitering at high altitude is over a very long distance.

Notice that the uplink and downlink distances can be expressed by $L_{\mathrm{G1U1}} = h_{\mathrm{UAV1}}/\cos(\zeta_{\mathrm{G1U1}})$ and $L_{\mathrm{U1G2}} = h_{\mathrm{UAV1}}/\cos(\zeta_{\mathrm{U1G2}})$, respectively. Using UAVs at high altitude, the total path length becomes approximately higher than 20 [km] (*i.e.*, $L_{\mathrm{G1U1}} + L_{\mathrm{U1G2}} > 20$ [km]) and under the effects of attenuation, turbulence, pointing error and AOA fluctuations it is a quite challenging distance for conventional FSO links. A considerable performance improvement with the application of RIS is also seen from Fig. 4. Another observation from Fig. 4 is the consistency of analytical and simulation results with the asymptotic ones. It is seen that the asymptotic analysis yields perfectly matched results to the exact and simulated ones, which show the accuracy of our analysis. This consistent trend not only validates the theoretical framework of our analysis, but also enhances reliability in the practical applicability of the obtained findings. However, the asymptotic results for high SNR regimes start to deviate from exact and simulation results when the average SNR falls below the lower bounds, *i.e.*, $\sim 20 - 40$ dB, depending on the selected parameters. The perfectly matched asymptotic results can also be seen in all next presented plots.

Fig. 5 - Fig. 7 show the variation of average BER versus various parameters. In Fig. 5, the average BER is illustrated depending on the field of view (FOV), reflection coefficient and number of RIS elements. We notice that larger FOV will enhance the BER performance but further increase of the FOV above a certain value does not maintain the performance improvement (*e.g.*, $\theta_{FOV} \gtrsim 60$ mrad). It is also seen from Fig. 5 that the application of RIS does not yield a performance improvement if FOV remains below a certain value (*e.g.*,

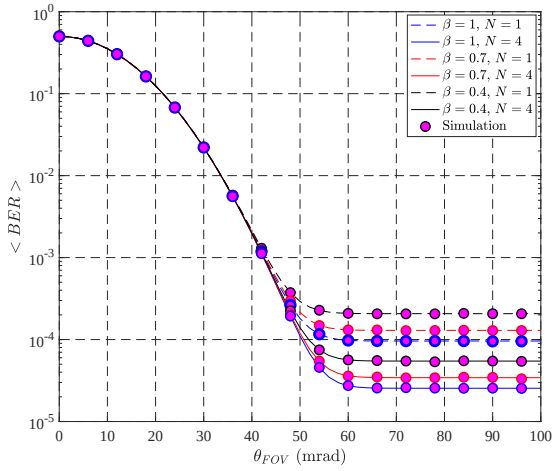

Fig. 5. One-UAV FSO path. BER versus the FOV angle in case of different reflection amplitudes and RIS elements.

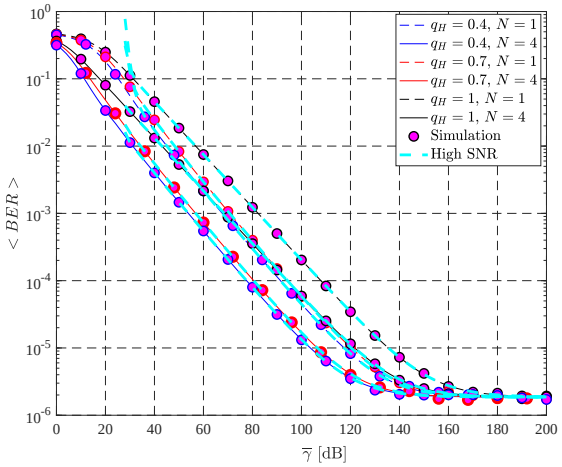

Fig. 6. One-UAV FSO path. BER versus the average SNR in case of different q_H values and RIS elements.

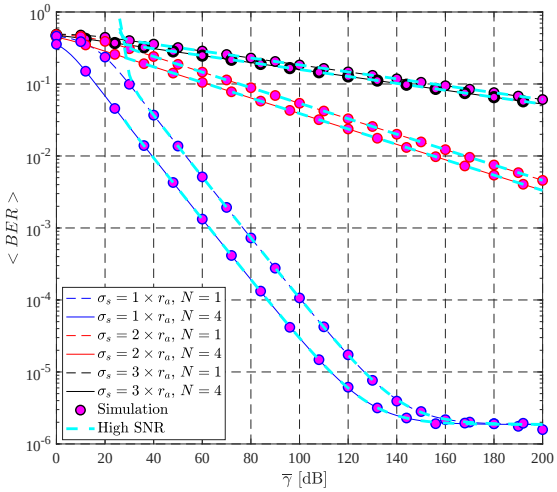

Fig. 7. One-UAV FSO path. BER versus the average SNR [dB] in case of different σ_s and RIS elements.

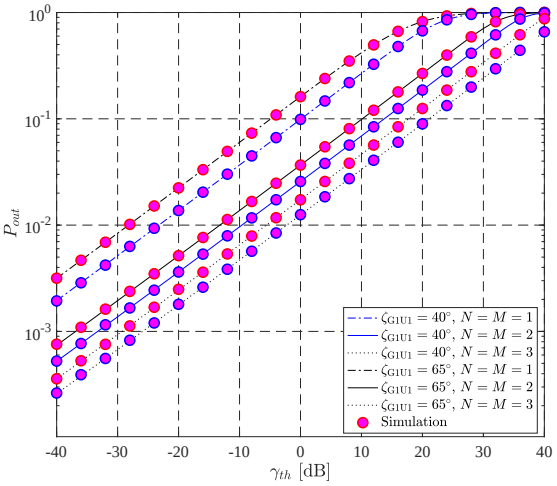

Fig. 8. Two-UAV FSO path. Outage probability versus the SNR threshold [dB] in case of different zenith angles, and RIS elements N and M for UAV1 and UAV2, respectively.

$\theta_{FOV} \lesssim 40$ mrad). It is well known that the reflectivity of RIS elements affects the efficiency of RIS application. In Fig. 5, keeping number of RIS elements as $N = 4$, if each RIS element is a perfect reflector *i.e.*, $\beta = 1$, then the average BER takes the value of $\sim 2.5 \times 10^{-5}$. However, average BER increases to $\sim 5.5 \times 10^{-5}$ when the reflection factor of each RIS element decreases to $\beta = 0.4$. In addition to using materials with higher reflection factor, the level of performance improvement can be extended by increasing the number of RIS elements. This can be verified with the change of average BER from $\sim 9.5 \times 10^{-5}$ to $\sim 2.5 \times 10^{-5}$ when the number of RIS increases from $N = 1$ to $N = 4$, while θ_{FOV} is equal to 70 mrad. Fig. 6 depicts the benefit of FSO communication system coming from asymmetrical behaviour of pointing error. The average BER is $\sim 5.3 \times 10^{-3}$ when beam misalignment is symmetrical (*e.g.*, $q_H = 1$); however average BER decreases to $\sim 1.4 \times 10^{-3}$ when the ratio of horizontal and vertical beam misalignments is $q_H = 0.4$ for average SNR $\overline{\gamma} = 50$ dB and $N = 4$. Finally, Fig. 7 investigates the impact of beam misalignment deviations on the BER performance. It can be observed that higher beam misalignment deviations cause significant performance degradation as expected. It is also seen that performance enhancement with the application of RIS stands at higher level when beam misalignment is smaller.

B. Performance of RIS-embedded two-UAVs FSO Path

In this section, we utilize the analytical results of outage probability and average BER for two-UAV RIS-assisted FSO communication system. It should be noted that N and M represents the number of RIS elements mounted on UAV1 and UAV2, respectively.

Fig. 8 illustrates the outage performance of two-UAV FSO communication system versus the SNR threshold, uplink zenith angle (*i.e.*, from GS1 to UAVs) and the number of RIS elements. Increasing the SNR threshold values results in the increase of outage probability. The outage probability remains at the high level with the increasing of zenith angle ζ_{G1U1}, hence increasing the link length L_{G1U1}. It is also highlighted

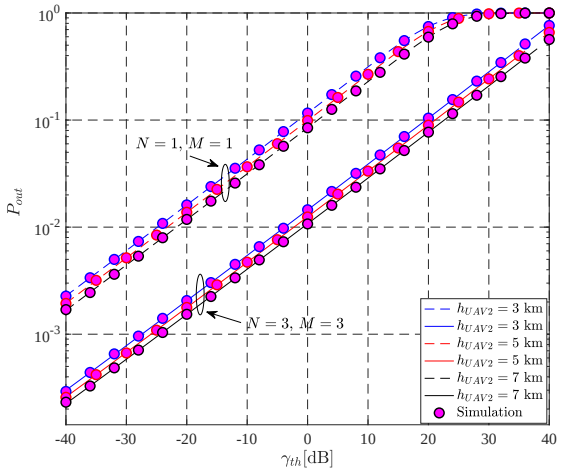

Fig. 9. Two-UAV FSO path. Outage probability versus the SNR threshold [dB] in case of different UAVs' altitudes, and RIS elements N and M for UAV1 and UAV2, respectively.

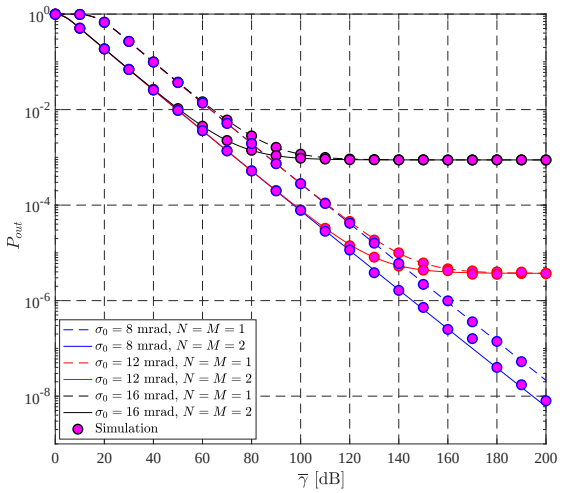

Fig. 10. Two-UAV FSO path. Outage probability versus the average SNR threshold [dB] in case of different beam curvature variances, and RIS elements N and M for UAV1 and UAV2, respectively.

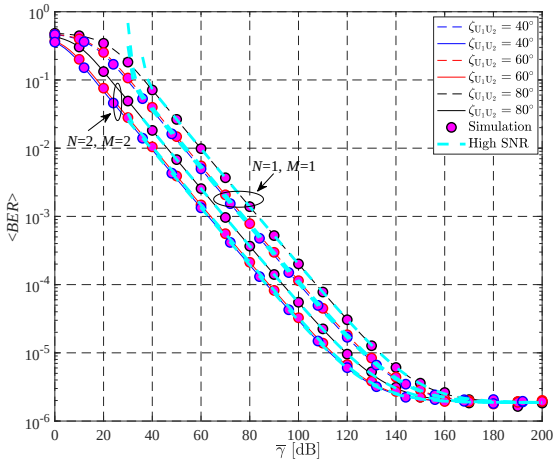

Fig. 11. Two-UAV FSO path. BER versus the average SNR [dB] in case of different UAVs' zenith angles, and RIS elements N and M for UAV1 and UAV2, respectively.

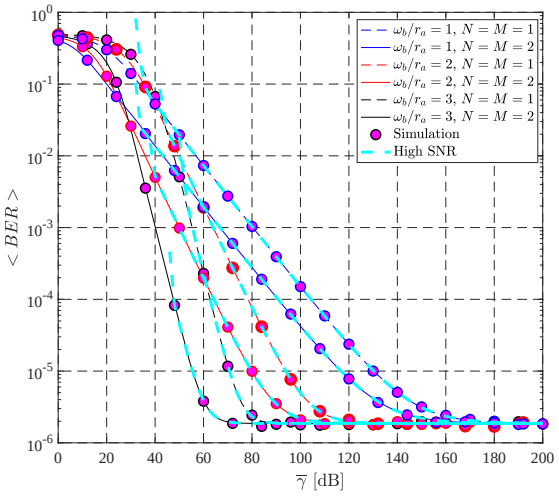

Fig. 12. Two-UAV FSO path. Outage probability versus the average SNR [dB] in case of different ratio ω_b/r_a, and RIS elements N and M for UAV1 and UAV2, respectively

in Fig. 8 that mounting RIS elements on both UAVs causes a meaningful decrease in the outage probability. On setting $\gamma_{th} = -10$ [dB] and $\zeta_{\text{G1U1}} = 40°$, the outage probability takes the values of $\sim 3.6 \times 10^{-2}$, $\sim 9.6 \times 10^{-3}$ and $\sim 4.6 \times 10^{-3}$ for $N = 1, M = 1$, $N = 2, M = 2$ and $N = 3, M = 3$, respectively.

In Fig. 9, the altitude of UAV1 is fixed to 10 [km] and the effect of altitude of UAV2 is investigated. As shown in Fig. 9, if the altitude of second hop is closer to the altitude of first hop, the outage performance improves more. The effect of orientation deviations, and hence the AOA fluctuations on outage performance of two-UAV RIS-assisted FSO communication system is demonstrated in Fig. 10. It can be inferred from Fig. 10 that the outage performance is strongly dependent on the AOA fluctuations. When the orientation deviation is small (*e.g.*, $\sigma_0 = 8$ mrad), the outage performance continues to improve with the RIS application and the SNR increase. However, for higher values of orientation deviations (*e.g.*, $\sigma_0 = 16$ mrad), outage performance improves up to certain level of average SNR (*i.e.*, $\overline{\gamma} > 100$ dB) then remains unchanged. Furthermore, the effect of zenith angle between two UAVs ζ_{U1U2} on the performance of FSO communication is depicted in Fig.11. We observe that smaller values of zenith angle causes decrease in the average BER.

Fig. 12 exhibits the variation of average BER depending on the average SNR, beam waist and number of RIS elements. The influence of beam waist on average BER is observed to be performance enhancing since the the probability of irradiance falls on the surfaces increases with the beam waist. Using $N = 2$ and $M = 2$ RIS elements pulls down the average BER value quickly, as compared to the $N = 1$ and $M = 1$ single surface case. The performance improvement remains higher for the higher values of beam waist, and it can be seen the decrease of average BER from $\sim 5 \times 10^{-3}$ to $\sim 4.6 \times 10^{-5}$ with the increase of number of RISs from $N = 1, M = 1$ to $N = 1, M = 1$ when the average SNR is fixed to $\overline{\gamma} = 50$ [dB].

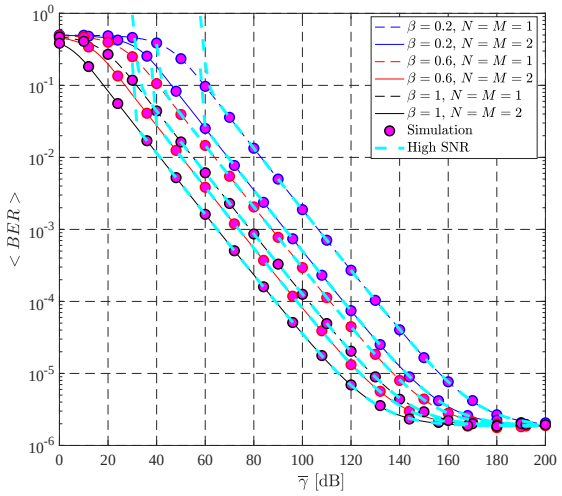

Fig. 13. Two-UAV FSO path. BER versus the average SNR [dB] in case of different reflection amplitudes and RIS elements N and M.

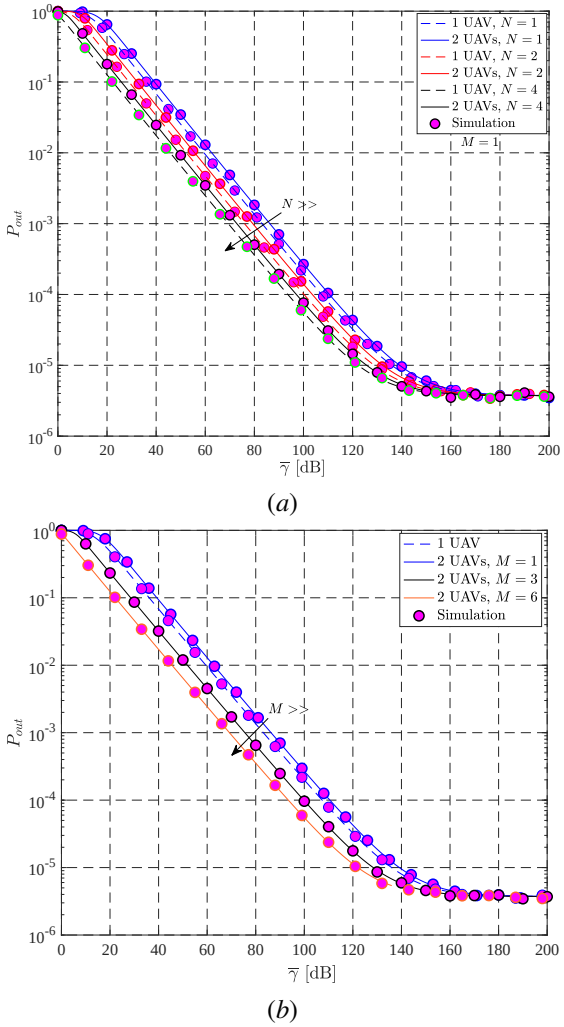

Fig. 14. Comparison of the outage probability for one and two UAV path, versus the average SNR [dB] and in case of different RIS elements *i.e.*, (*a*) variable N, and (*b*) fixed $N = 1$ with variable M.

The dependency of outage and BER performances for the two-UAV FSO path is on the square of reflection factor β, as it can be seen from Eqs. (45). Fig. 13 denotes the dependency of average BER on the reflection factor and the number of RIS elements. Since optical signal reflects from surfaces twice, the performance of two UAVs FSO communication system degrades with the β^2, and hence the error probability will be inversely proportional to β^2. Keeping the number of RIS elements as $N = 2, M = 2$ and average SNR as $\overline{\gamma} = 100$ [dB], the average BER increases from $\sim 3.5 \times 10^{-5}$ to $\sim 5 \times 10^{-4}$ with the decrease of reflection factor from $\beta = 1$ to $\beta = 0.2$, which shows the importance of keeping reflectivity of the surface materials higher. The comparison between two FSO paths is well described in Fig. 14 in case of the outage probability for different numbers of RIS elements. We set the number of RIS elements mounted on the second UAV to $M = 1$ and changed only the number of RIS elements on the first UAV. It was observed that the outage performance for one-UAV path always remains better than that of two-UAVs when the number of RISs on the second UAV is $M = 1$. This shows that the second UAV with single RIS cell acts like a bottleneck regardless of the number of RIS cells in the first UAV. However, the benefits of using multiple UAVs is highlighted in Fig. 14(*b*), where we fixed the number of RISs on the first UAV to $N = 1$. Although, it was seen that one-UAV path yields better performance as compared to two-UAVs when the number of RIS on the second UAV is $M = 1$, when $M \geq 2$ the two-UAVs path shows better performance than the one-UAV path. This allows to state that the multi-hop UAV path enhances the link performance in case of increasing number of RIS elements. For instance, an improvement of 10^{-1} is achieved when moving from a single UAV with $N = 1$ to two UAVs with $M = 6$ for $\overline{\gamma} = 50$ [dB].

The comparison of the average BER achieved through the two paths is shown in Fig. 15, for different number of RIS elements. It is seen that the average BER remains lower for $N = 1$ one-UAV than that of $N = 1, M = 1$ two-UAVs. However, the average BER starts to take the lowest value for two-UAVs path after increasing the number of RIS elements to $N = 2, M = 2$ that verifies the superiority of two-UAVs on the one-UAV FSO communication for the sufficient number of RIS elements. Finally, Fig. 16 depicts the effect of the number of RIS elements on BER and outage probability. As expected, for increasing SNR, performance improve, as well as for high values of RIS elements. Furthermore, in case of two-UAV path the number of element at the first UAV strongly affects the performance of the whole path. To provide a fair comparison between one- and two-UAV aided schemes with conventional scheme using UAV as relays and assess their practical deployment in terms of performance improvement, we present Fig. 17. It is observed that using UAV as a relay yields better performance than that of one- and two-UAV cases with $N = 1$ and $N = M = 1$ RIS elements. However, the performance of one- and two-UAV cases superior the UAV as relay case when the number of RIS elements increases. As for increasing number of RIS elements, it is noticed a gap between one UAV and two UAVs. However, this gap reduces for lower number of RIS elements.

It is known that RIS-aided FSO communication link suffers

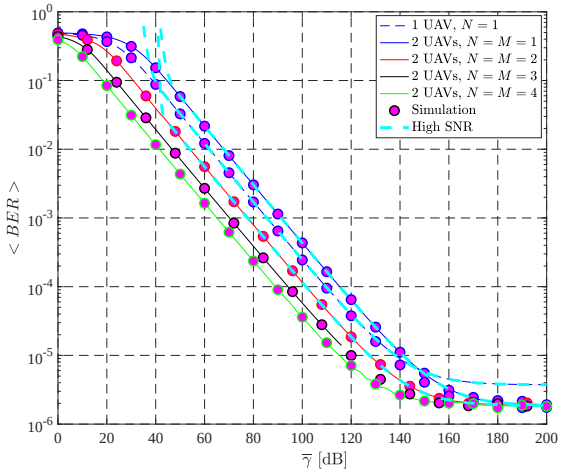

Fig. 15. Comparison of the BER for one- and two- UAV FSO path, versus the average SNR [dB], in case of different RIS elements.

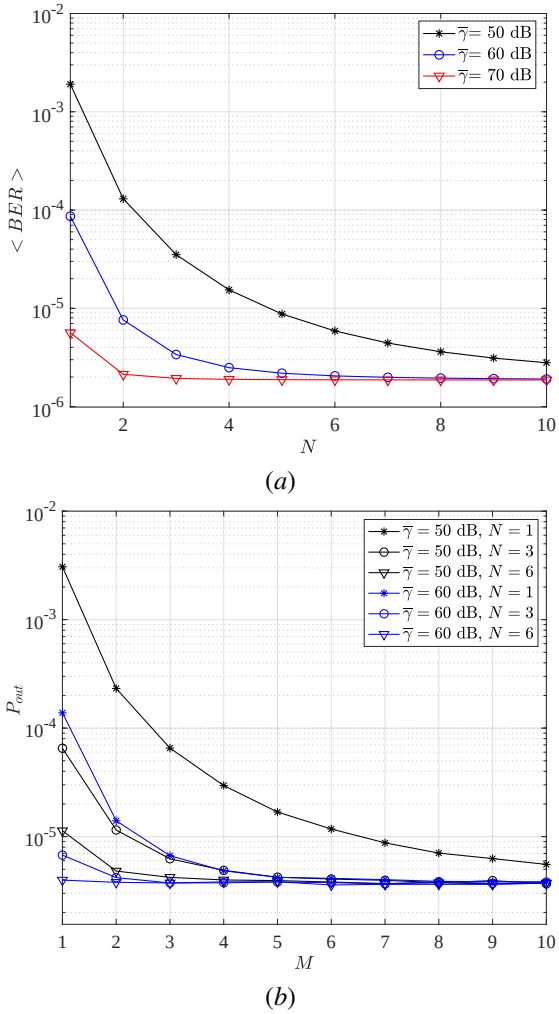

Fig. 16. Effect of the RIS elements on the BER and outage probability for different values of average SNR and in case of (*a*) one and (*b*) two UAV path, respectively.

from the double fading effect, which is commonly eased by a large number of elements or short distances from the RIS [39]. Since the FSO link has high attenuation, it is seen from the results given in this section that the RIS application works effectively in terms of improving both outage and average BER performance even with one element. One of the reasons of this effectiveness can be the assumption of RIS-induced phase shift compensation in this study, and hence coherently received signals achieved high gain with maximized SNR. Knowing that the short distances from RIS also triggers the fading effect, it is possible to not encounter the double fading effect since the UAV based communication link has longer distances, *e.g.*, $\sim 5 - 20$ km. However, it should be kept in mind that the remarkable performance improvement can be obtained when a higher number of surfaces are utilized, as observed from Fig. 12, 13, 14, and 15.

All presented results and discussions in this section imply that the benefit of RIS application for FSO communication link through both one-UAV and two-UAVs is undeniable. However, the application type of RIS can also yield a further performance improvement. In [39], a comparison of active and passive RIS application was given and it was shown that, due to its power amplification capability hence additional amplified power term in the SNR expression, the active RIS application outperforms the passive RIS-mounted FSO communication link. In the same work, it was also shown that the active RIS, which deals with the double fading effect, seems more suitable for the FSO communications due to less power attenuation. In [39], the asymptotic received SNR of active RIS remained almost ~ 40 dB higher than that of passive RIS application up to $\sim N = 1000$ RIS elements and the superiority of active RIS over passive RIS continued up to $\sim N = 2.5 \times 10^6$ RIS elements (such high number is not case in our work), after that passive RIS yielded better results. Finally, Fig. 18 depicts the outage probability achieved in case of two-UAV FSO path for different RIS elements, expressed as product $M \times N$. The trends are presented for different values of beamwaist, and as in Fig. 2, the outage probability decreases for high values of beamwaist. The asymptotic analysis is also reported in Fig. 18 for extremely large number of surfaces, showing a consistent trend with the outage probability obtained with simulations.

X. Conclusions

This paper investigates the use of RISs, embedded in UAVs for a multi-hop FSO data transmission in case of different attenuation losses, like atmospheric, pointing errors, and AOAs fluctuations. Our study focused on two possible paths, respectively with one and two UAVs. In both cases, we derived the BER and outage probability for different geometric parameters and number of RIS elements. It has been noticed that for high number of RIS elements the performance improves, as well as for multi-UAVs data propagation. We then envision the possibility to extend our proposed model to guarantee connectivity through a swarm of UAVs, able to tune a wireless signal, in order to reach skip-zones. The proposed architecture is intended for backhaul data transmission, able to connect ground stations that are not in LoS, through UAVs accordingly equipped with RISs. The use of multi-hop RIS-embedded UAV paths results a viable approach for optimal link management.

Finally, in this paper, passive RIS application is considered. According to the above aforementioned evaluations and results

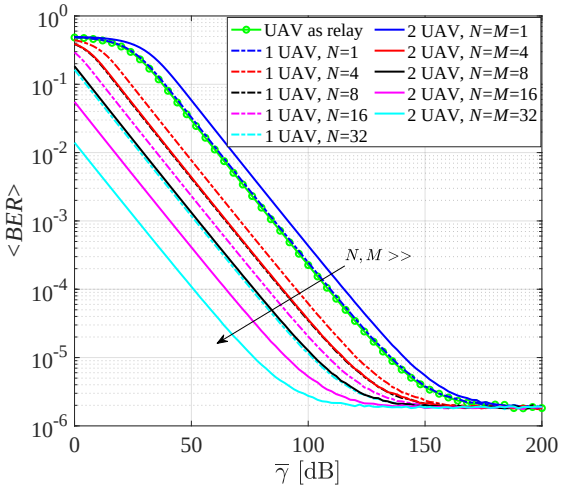

Fig. 17. Comparison of the BER for one- and two-UAV FSO path to the case of UAV as relay node, versus the average SNR [dB], in case of different RIS elements.

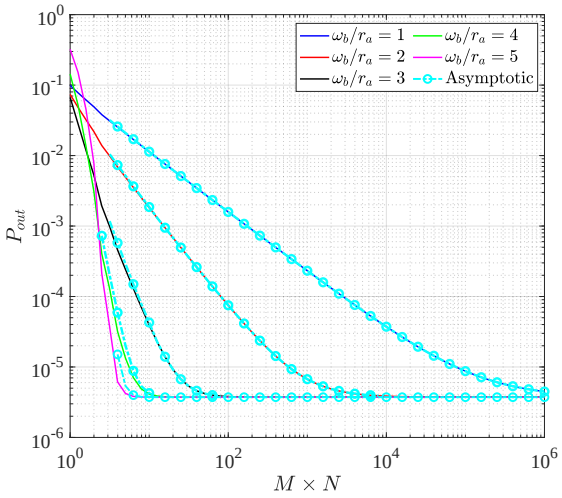

Fig. 18. Outage probability versus different numbers of RIS elements in case of two-UAV FSO path.

presented in [39], it is obvious that active RIS-assisted FSO communication through UAV will yield better performance. Indeed, active RIS provides dynamic beamforming, interference mitigation, and adaptive link optimization, while passive RIS offers energy-efficient operation and reduced complexity. By leveraging the complementary strengths of active and passive RIS, FSO systems can achieve improved performance, reliability, and flexibility in diverse operating scenarios.

ACKNOWLEDGMENT

This article is partially based on work from COST Action NEWFOCUS CA19111, supported by COST (European Cooperation in Science and Technology).

APPENDIX A
CHANNEL PDF DERIVATION

Inserting Eq. (5) and (33) into Eq. (34) and adopting the small angle approximation *i.e.*, $\cos(\theta_d) \approx 1$, that is also adopted in [31], we can write

$$f_h(h) = \underbrace{\frac{\eta_s^2 (b-1)^b h^{-1-b}}{2\pi q_H \mathfrak{B}(a,b) a^b (A_0 h_{al})^{-b} \Gamma(a+b)}}_{\mathcal{A}} \int_{-\pi}^{\pi} d\varphi \times \underbrace{G_{2,2}^{2,1}\left(\frac{a}{(b-1) A_0 h_{al}} h \middle| \begin{matrix} 1, b+\eta_s^2 \xi(\varphi)+1 \\ a+b, b+\eta_s^2 \xi(\varphi) \end{matrix} \right)}_{\mathcal{B}} \times \underbrace{\frac{1}{\sigma_0^2} \int_0^{\theta_{FOV}} \theta_d \exp\left(-\theta_d^2/(2\sigma_0^2)\right) d\theta_d}_{\mathcal{C}} + \frac{\delta(h)}{\sigma_0^2} \int_{\theta_{FOV}}^{\infty} \theta_d \exp\left(-\theta_d^2/(2\sigma_0^2)\right) d\theta_d. \tag{A.1}$$

To solve the last integral given in Eq. (A.1), we can use the expression given by Eq. (3.381-9) of [33] with $v = (m+1)/n$, $\mathfrak{Re}[n] > 0$ and $\mathfrak{Re}[\beta] > 0$. Furthermore, to solve the θ_d-dependent integral in $\mathcal{C}$, we use the expression given in Eq. (3.381-8) of [33]. Finally, Eq. (A.1) becomes *i.e.*,

$$f_h(h) = \mathcal{A} \int_{-\pi}^{\pi} \mathcal{B} d\varphi \gamma\left(1, \frac{\theta_{FOV}^2}{2\sigma_0^2}\right) + \delta(h) \exp\left(-\frac{\theta_{FOV}^2}{2\sigma_0^2}\right), \tag{A.2}$$

where $\gamma(a,x) = \int_0^x e^{-t} t^{a-1} dt$ is the lower incomplete Gamma function. Finally, by replacing the conversion of $\gamma(a,x)$, Eq. (A.2) can be written as *i.e.*,

$$f_h(h) = \mathcal{A}\left[1 - \exp\left(-\frac{\theta_{FOV}^2}{2\sigma_0^2}\right)\right] h^{-b-1} \int_{-\pi}^{\pi} \mathcal{B} d\varphi + \delta(h) \exp\left(-\theta_{FOV}^2/(2\sigma_0^2)\right). \tag{A.3}$$

APPENDIX B
CDF AND OUTAGE PROBABILITY DERIVATIONS IN CASE OF ONE-UAV FSO PATH

In order to obtain the CDF of the SNR, we can replace Eq. (36) in the expression $F_\gamma(\gamma) = \int_0^\gamma f_\gamma(x) dx$, so we obtain

$$F_\gamma(\gamma) = \frac{\eta_s^2 (b-1)^b \left[1 - \exp\left(-\frac{\theta_{FOV}^2}{2\sigma_0^2}\right)\right]}{2\pi q_H \Gamma(a)\Gamma(b) a^b (A_0 h_{al})^{-b}} \int_{-\pi}^{\pi} d\varphi \times \frac{1}{2(N\mathcal{B})^{-b} \bar{\gamma}^{-b/2}} \int_0^\gamma x^{-b/2-1} \times G_{2,2}^{2,1}\left(\frac{a(b-1)^{-1}\sqrt{x}}{A_0 h_{al} \sqrt{\bar{\gamma}} N\mathcal{B}} \middle| \begin{matrix} 1, b+\eta_s^2 \xi(\varphi)+1 \\ a+b, b+\eta_s^2 \xi(\varphi) \end{matrix} \right) dx + \frac{\exp\left(-\frac{\theta_{FOV}^2}{2\sigma_0^2}\right)}{2N\mathcal{B}\sqrt{\bar{\gamma}}} \int_0^\gamma \frac{1}{\sqrt{x}} \delta\left(\frac{\sqrt{x}}{\sqrt{\bar{\gamma}} N\mathcal{B}}\right) dx. \tag{B.1}$$

To solve the last integral in Eq. (B.1), we can use the following variable *i.e.*, $t = \sqrt{x}/\sqrt{\bar{\gamma}} N\mathcal{B}$, and the integral becomes 1.

In order to solve the x-dependent integral, we use Eq. 26 from [34] and exploit some mathematical calculations, then having

$$F_\gamma(\gamma) = \frac{\eta_s^2 (b-1)^b (A_0 h_{al} N\mathcal{B}\sqrt{\overline{\gamma}})^b \left[1-\exp\left(-\frac{\theta_{FOV}^2}{2\sigma_0^2}\right)\right]}{2\pi q_H \Gamma(a)\Gamma(b) a^b (\sqrt{\gamma})^b} \times \int_{-\pi}^{\pi} G_{3,3}^{2,2}\left(\frac{a\sqrt{\gamma}}{(b-1) A_0 h_{al}\sqrt{\overline{\gamma}} N\mathcal{B}}\middle|\begin{matrix}\Psi_1,\Psi_2,\Psi_3\\ \Psi_4,\Psi_5,\Psi_6\end{matrix}\right) d\varphi + \exp\left(-\theta_{FOV}^2/(2\sigma_0^2)\right), \tag{B.2}$$

where $\{\Psi_1,\Psi_2,\Psi_3,\Psi_4,\Psi_5,\Psi_6\} = \{1, 1+b, b+\eta_s^2\xi(\varphi)+1, a+b, b+\eta_s^2\xi(\varphi), b\}$. According to Eq. (37), the outage probability can be found as

$$P_{out} = \frac{\eta_s^2 (A_0 h_{al} N\mathcal{B}\sqrt{\overline{\gamma}})^b \left[1-\exp\left(-\frac{\theta_{FOV}^2}{2\sigma_0^2}\right)\right]}{2\pi (b-1)^{-b} q_H \Gamma(a)\Gamma(b) a^b (\sqrt{\gamma_{th}})^b} \times \int_{-\pi}^{\pi} G_{3,3}^{2,2}\left(\frac{a (b-1)^{-1}\sqrt{\gamma_{th}}}{A_0 h_{al}\sqrt{\overline{\gamma}} N\mathcal{B}}\middle|\begin{matrix}\Psi_1,\Psi_2,\Psi_3\\ \Psi_4,\Psi_5,\Psi_6\end{matrix}\right) d\varphi + \exp\left(-\theta_{FOV}^2/(2\sigma_0^2)\right). \tag{B.3}$$

Appendix C
BER Derivation in case of One-UAV FSO Path

Considering Eq. (40), we can solve the second part of the integral assuming the variable $t = \sqrt{\gamma}/\left(\sqrt{\overline{\gamma}} N\mathcal{B}\right)$, *i.e.*,

$$P_b(e) = \underbrace{\frac{\eta_s^2 (b-1)^b \left[1-\exp\left(-\frac{\theta_{FOV}^2}{2\sigma_0^2}\right)\right]}{8\pi q_H \Gamma(a)\Gamma(b) a^b (A_0 h_{al} N\mathcal{B})^{-b} \overline{\gamma}^{-b/2}}}_{\mathcal{A}} \times \int_{-\pi}^{\pi} d\varphi \int_0^{\infty} \gamma^{-b/2-1} \operatorname{erfc}\left(\frac{\sqrt{\gamma}}{2}\right) d\gamma \times \underbrace{G_{2,2}^{2,1}\left(\frac{a (b-1)^{-1}\sqrt{\gamma}}{A_0 h_{al}\sqrt{\overline{\gamma}} N\mathcal{B}}\middle|\begin{matrix}1, b+\eta_s^2\xi(\varphi)+1\\ a+b, b+\eta_s^2\xi(\varphi)\end{matrix}\right)}_{\mathcal{B}} + 0.5\exp\left(-\theta_{FOV}^2/(2\sigma_0^2)\right)/(2N\mathcal{B}\sqrt{\overline{\gamma}}) \times \int_0^{\infty} \operatorname{erfc}\left(\frac{\sqrt{\overline{\gamma}} N\mathcal{B} t}{2}\right)\delta(t) 2\sqrt{\overline{\gamma}} N\mathcal{B} dt. \tag{C.1}$$

Since $\int_0^{\infty} \delta(t)\operatorname{erfc}\left(\frac{\sqrt{\overline{\gamma}} N\mathcal{B} t}{2}\right) dt = \operatorname{erfc}(0) = 1$, and posing $\operatorname{erfc}(\sqrt{x}) = \frac{1}{\sqrt{\pi}} G_{1,2}^{2,0}\left(x\middle|\begin{matrix}1\\ 0, 1/2\end{matrix}\right)$ [40], Eq. (C.1) becomes

$$P_b(e) = \frac{\mathcal{A}}{\sqrt{\pi}} \int_{-\pi}^{\pi}\int_0^{\infty} d\varphi\gamma^{-b/2-1} G_{1,2}^{2,0}\left(\frac{1}{4}\gamma\middle|\begin{matrix}1\\ 0, 1/2\end{matrix}\right)\mathcal{B} + 0.5\exp\left(-\theta_{FOV}^2/(2\sigma_0^2)\right). \tag{C.2}$$

Finally, through Eq. (07.34.21.0013.01) and then applying Eq. (07.34.16.0001.01) of [35], we can obtain the following expression of error probability as given in Eq. (41).

Appendix D
CDF and Outage Probability Derivations in case of Two-UAV FSO Path

Considering the expression $F_\gamma(\gamma) = \int_0^{\gamma} f_\gamma(x)dx$, we can replace Eq. (43) in order to obtain:

$$F_\gamma(\gamma) = \underbrace{\frac{\eta_s^2 (b-1)^b \left[1-\exp\left(-\frac{\theta_{FOV}^2}{2\sigma_0^2}\right)\right]}{4\pi q_H \Gamma(a)\Gamma(b) a^b (A_0 h_{al}\sqrt{\overline{\gamma}} MN\mathcal{B}^2)^{-b}}}_{\mathcal{A}} \int_{-\pi}^{\pi} d\varphi \int_0^{\gamma} x^{-\frac{b}{2}-1} \times \underbrace{G_{2,2}^{2,1}\left[\frac{a(b-1)^{-1}\sqrt{x}}{A_0 h_{al}\sqrt{\overline{\gamma}} MN\mathcal{B}^2}\middle|\begin{matrix}1, b+\eta_s^2\xi(\varphi)+1\\ a+b, b+\eta_s^2\xi(\varphi)\end{matrix}\right]}_{\mathcal{B}} dx + \frac{\exp\left(-\frac{\theta_{FOV}^2}{2\sigma_0^2}\right)}{2\sqrt{\overline{\gamma}} MN\mathcal{B}^2} \int_0^{\gamma} \frac{1}{\sqrt{x}}\delta\left(\frac{\sqrt{x}}{\sqrt{\overline{\gamma}} MN\mathcal{B}^2}\right) dx. \tag{D.1}$$

We rely on the variable $t = \sqrt{x}/\left(\sqrt{\overline{\gamma}} MN\mathcal{B}^2\right)$ to solve the last integral in Eq. (D.1). Also, to solve the x-dependent integral, we exploit a variable change *i.e.*, $t = \sqrt{x} \Rightarrow dx = 2tdt$, and use Eq. 26 from [34]. It follows that Eq. (D.1) will be:

$$F_\gamma(\gamma) = \exp\left(-\theta_{FOV}^2/(2\sigma_0^2)\right) + 2\mathcal{A}\int_{-\pi}^{\pi} d\varphi\left(\sqrt{\gamma}\right)^{-b} \times \underbrace{G_{3,3}^{2,2}\left[\frac{a(b-1)^{-1}\sqrt{\gamma}}{A_0 h_{al}\sqrt{\overline{\gamma}} MN\mathcal{B}^2}\middle|\begin{matrix}\Psi_1,\Psi_2,\Psi_3\\ \Psi_4,\Psi_5,\Psi_6\end{matrix}\right]}_{\mathcal{C}}, \tag{D.2}$$

where $\{\Psi_1,..,\Psi_6\}$ are given in Eq. (B.2). Finally, the outage probability can be rewritten as given in Eq. (44).

Appendix E
BER Derivation in case of Two-UAV FSO Path

From Eq. (43), we can insert the PDF of SNR in Eq. (39) and obtain

$$P_b(e) = \underbrace{\frac{\eta_s^2 (b-1)^b \left[1-\exp\left(-\frac{\theta_{FOV}^2}{2\sigma_0^2}\right)\right]}{8\pi q_H \Gamma(a)\Gamma(b) a^b (A_0 h_{al}\sqrt{\overline{\gamma}} MN\mathcal{B}^2)^{-b}}}_{\mathcal{A}} \times \int_{-\pi}^{\pi} d\varphi \int_0^{\infty} \gamma^{-b/2-1}\operatorname{erfc}\left(\frac{\sqrt{\gamma}}{2}\right) d\gamma \times \underbrace{G_{2,2}^{2,1}\left[\frac{a(b-1)^{-1}\sqrt{\gamma}}{A_0 h_{al}\sqrt{\overline{\gamma}} MN\mathcal{B}^2}\middle|\begin{matrix}1, b+\eta_s^2\xi(\varphi)+1\\ a+b, b+\eta_s^2\xi(\varphi)\end{matrix}\right]}_{\mathcal{B}} + \frac{\exp\left(-\frac{\theta_{FOV}^2}{2\sigma_0^2}\right)}{4\sqrt{\overline{\gamma}} MN\mathcal{B}^2} \int_0^{\infty} \frac{\operatorname{erfc}\left(\frac{\sqrt{\gamma}}{2}\right)}{\sqrt{\gamma}}\delta\left(\frac{\sqrt{\gamma}}{\sqrt{\overline{\gamma}} MN\mathcal{B}^2}\right) d\gamma. \tag{E.1}$$

To solve the last integral in Eq. (E.1), we pose $t = \sqrt{\gamma}/\left(\sqrt{\overline{\gamma}} MN\mathcal{B}^2\right)$, and replace $\int_0^{\infty}\delta(t)\operatorname{erfc}\left(\frac{\sqrt{\overline{\gamma}} MN\mathcal{B}^2 t}{2}\right) dt =$

$\operatorname{erfc}(0) = 1$. Through Eq. (07.34.21.0013.01) and applying Eq. (07.34.16.0001.01) of [35], Eq. (E.1) becomes:

$$\begin{aligned} P_b(e) = & \frac{2^{a+b-1}\eta_s^2\left[1-\exp\left(-\frac{\theta_{FOV}^2}{2\sigma_0^2}\right)\right]}{16\pi^2\sqrt{\pi}q_H\Gamma(a)\Gamma(b)} \int_{-\pi}^{\pi} d\varphi \\ & \times G_{6,5}^{4,4}\left(\frac{4a^2(b-1)^{-2}}{\left(A_0 h_{al}\sqrt{\bar{\gamma}}MN\mathcal{B}\right)^2}\middle|\begin{matrix}\Delta_{1,1},..,\Delta_{1,6}\\ \Delta_{2,1},..,\Delta_{2,5}\end{matrix}\right) \\ & + 0.5\exp\left(-\theta_{FOV}^2/(2\sigma_0^2)\right), \end{aligned} \tag{E.2}$$

where $\Delta_{1,1},\ldots,\Delta_{1,6}$ and $\Delta_{2,1},\ldots,\Delta_{2,5}$ are defined in Eq. (41).

REFERENCES

[1] G. Oliveri, A. Benoni, P. Rocca, M. Salucci, and A. Massa, "RIS Dynamic Control Strategies in Smart EM Environments for 6G Networks," in *2023 17th European Conference on Antennas and Propagation (EuCAP)*, 2023, pp. 1–3.

[2] Q. Wu and R. Zhang, "Intelligent Reflecting Surface Enhanced Wireless Network via Joint Active and Passive Beamforming," *IEEE Trans. on Wireless Communications*, vol. 18, no. 11, pp. 5394–5409, 2019.

[3] E. Basar, M. Di Renzo, J. De Rosny, M. Debbah, M.-S. Alouini, and R. Zhang, "Wireless Communications Through Reconfigurable Intelligent Surfaces," *IEEE Access*, vol. 7, pp. 116 753–116 773, 2019.

[4] Q. Wu and R. Zhang, "Towards Smart and Reconfigurable Environment: Intelligent Reflecting Surface Aided Wireless Network," *IEEE Communications Magazine*, vol. 58, no. 1, pp. 106–112, 2020.

[5] M. D. Renzo *et al.*, "Smart radio environments empowered by reconfigurable AI meta-surfaces: an idea whose time has come ," *J. Wireless Com Network*, vol. 129, 2019.

[6] C. Pan *et al.*, "An overview of signal processing techniques for ris/irs-aided wireless systems," *IEEE Journal of Selected Topics in Signal Processing*, vol. 16, no. 5, pp. 883–917, 2022.

[7] B. Ji, Y. Han, S. Liu, F. Tao, G. Zhang, Z. Fu, and C. Li, "Several Key Technologies for 6G: Challenges and Opportunities," *IEEE Communications Standards Magazine*, vol. 5, no. 2, pp. 44–51, 2021.

[8] S. Aboagye, A. R. Ndjiongue, T. M. N. Ngatched, O. A. Dobre, and H. V. Poor, "RIS-Assisted Visible Light Communication Systems: A Tutorial," *IEEE Communications Surveys & Tutorials*, vol. 25, no. 1, pp. 251–288, 2023.

[9] A. R. Ndjiongue, T. M. N. Ngatched, O. A. Dobre, and H. Haas, "Symbolic Representation of RIS-Assisted FSO Channels," in *2022 IEEE Globecom Workshops (GC Wkshps)*, 2022, pp. 1778–1783.

[10] Y. Zhang, M. A. Kishk, and M.-S. Alouini, "Hap-enabled communications in rural areas: When diverse services meet inadequate communication infrastructures," *IEEE Open Journal of the Communications Society*, vol. 4, pp. 2274–2285, 2023.

[11] L. Yang, W. Guo, and I. S. Ansari, "Mixed Dual-Hop FSO-RF Communication Systems Through Reconfigurable Intelligent Surface," *IEEE Communications Letters*, vol. 24, no. 7, pp. 1558–1562, 2020.

[12] V. K. Chapala and S. M. Zafaruddin, "Reconfigurable Intelligent Surface Empowered Multi-Hop Transmission over Generalized Fading," in *2022 IEEE 95th Vehicular Technology Conference: (VTC2022-Spring)*, 2022, pp. 1–5.

[13] K. Zhi, C. Pan, H. Ren, and K. Wang, "Power scaling law analysis and phase shift optimization of RIS-aided massive MIMO systems with statistical CSI," *IEEE Transactions on Communications*, vol. 70, no. 5, pp. 3558–3574, 2022.

[14] K. Zhi, C. Pan, H. Ren, K. Wang, M. Elkashlan, M. Di Renzo, R. Schober, H. V. Poor, J. Wang, and L. Hanzo, "Two-timescale design for reconfigurable intelligent surface-aided massive mimo systems with imperfect csi," *IEEE Transactions on Information Theory*, 2022.

[15] X. Li, Y. Li, X. Song, L. Shao, and H. Li, "RIS Assisted UAV for Weather-Dependent Satellite Terrestrial Integrated Network With Hybrid FSO/RF Systems," *IEEE Photonics Journal*, vol. 15, no. 5, pp. 1–17, 2023.

[16] Y. Ata and M.-S. Alouini, "Performance of Integrated Ground-Air-Space FSO Links Over Various Turbulent Environments," *IEEE Photonics Journal*, vol. 14, no. 6, pp. 1–16, 2022.

[17] ——, "HAPS Based FSO Links Performance Analysis and Improvement With Adaptive Optics Correction," *IEEE Trans. on Wireless Communications*, vol. 22, no. 7, pp. 4916–4929, 2023.

[18] A. R. Ndjiongue, T. M. N. Ngatched, O. A. Dobre, and H. Haas, "Design of a Power Amplifying-RIS for Free-Space Optical Communication Systems," *IEEE Wireless Communications*, vol. 28, no. 6, pp. 152–159, 2021.

[19] R. P. Naik, P. Krishnan, and G. D. G. Simha, "Reconfigurable Intelligent Surface-assisted Free-Space Optical Communication System under the Influence of Signal Blockage for Smart-city Applications," *Applied Optics*, vol. 61, no. 20, pp. 5957–5964, 2022.

[20] A. C. Pogaku, D.-T. Do, B. M. Lee, and N. D. Nguyen, "UAV-Assisted RIS for Future Wireless Communications: A Survey on Optimization and Performance Analysis," *IEEE Access*, vol. 10, pp. 16 320–16 336, 2022.

[21] H. Jia, J. Zhong, M. N. Janardhanan, and G. Chen, "Ergodic Capacity Analysis for FSO Communications with UAV-Equipped IRS in the Presence of Pointing Error," in *2020 IEEE 20th International Conference on Communication Technology (ICCT)*, 2020, pp. 949–954.

[22] J. Luo, T. Liang, C. Chen, and T. Zhang, "A UAV mounted RIS aided communication and localization integration system for ground vehicles," in *2022 IEEE International Conference on Communications Workshops (ICC Workshops)*, 2022, pp. 139–144.

[23] E. Hanbay and G. Altın, "UAV-Assisted Wireless Communication System with Reconfigurable Intelligent Surfaces: Outage Probability Approach," in *2022 Intl. Conf. on Innovation and Intelligence for Informatics, Computing, and Technologies (3ICT)*, 2022, pp. 112–116.

[24] T. V. Nguyen, H. D. Le, and A. T. Pham, "On the Design of RIS–UAV Relay-Assisted Hybrid FSO/RF Satellite–Aerial–Ground Integrated Network," *IEEE Trans. on Aerospace and Electronic Systems*, vol. 59, no. 2, pp. 757–771, 2023.

[25] L. Han, X. Liu, Y. Wang, and X. Hao, "Analysis of RIS-Assisted FSO Systems Over $\mathcal{F}$-Turbulence Channel With Pointing Errors and Imperfect CSI," *IEEE Wireless Communications Letters*, vol. 11, no. 9, pp. 1940–1944, 2022.

[26] L. De Lucia, C. E. Palazzi, and A. M. Vegni, "ENSING: Energy saving based data transmission in Internet of Drones for 3D connectivity in 6G networks," *Ad Hoc Networks*, vol. 149, p. 103211, 2023.

[27] M. C. A. Naboulsi, H. Sizun, and F. de Fornel, "Fog Attenuation Prediction for Optical and Infrared Waves," *Optical Engineering*, vol. 43, no. 2, pp. 319 – 329, 2004. [Online]. Available: https://doi.org/10.1117/1.1637611

[28] L. C. Andrews and R. L. Phillips, *Laser Beam Propagation through Random Media*. Bellingham: SPIE, 2005.

[29] K. P. Peppas, G. C. Alexandropoulos, E. D. Xenos, and A. Maras, "The fischer–snedecor $\mathcal{F}$-distribution model for turbulence-induced fading in free-space optical systems," *Journal of Lightwave Technology*, vol. 38, no. 6, pp. 1286–1295, 2020.

[30] W. Gappmair, S. Hranilovic, and E. Leitgeb, "OOK Performance for Terrestrial FSO Links in Turbulent Atmosphere with Pointing Errors Modeled by Hoyt Distributions," *IEEE Communications Letters*, vol. 15, no. 8, pp. 875–877, 2011.

[31] H. Safi, A. Dargahi, J. Cheng, and M. Safari, "Analytical Channel Model and Link Design Optimization for Ground-to-HAP Free-Space Optical Communications," *Journal of Lightwave Technology*, vol. 38, no. 18, pp. 5036–5047, 2020.

[32] O. S. Badarneh *et al.*, "On the Sum of Fisher–Snedecor $\mathcal{F}$ Variates and Its Application to Maximal-Ratio Combining," *IEEE Wireless Communications Letters*, vol. 7, no. 6, pp. 966–969, 2018.

[33] I. S. Gradshteyn and I. M. Ryzhik, *Table of Integrals, Series, and Products*. London: Elsevier, 2014.

[34] V. S. Adamchik and O. I. Marichev, "The algorithm for calculating integrals of hypergeometric type functions and its realization in reduce system," in *Intl. Symp. on Symbolic and Algebraic Computation*, 1990.

[35] "The Mathematical Functions Site, Wolfram Inc." https://functions.wolfram.com/, accessed: 2023-10-07.

[36] A. A. Kilbas, *H-transforms: Theory and Applications*. CRC press, 2004.

[37] P. Milsom, "A ray-optic, Monte Carlo, description of a Gaussian beam waist–applied to reverse saturable absorption," *Applied Physics B*, vol. 70, no. 4, pp. 593–599, 2000.

[38] J. Ricklin, W. Miller, and L. Andrews, "Effective beam parameters and the turbulent beam waist for convergent gaussian beams," *Applied optics*, vol. 34, no. 30, pp. 7059–7065, 1995.

[39] K. Zhi, C. Pan, H. Ren, K. K. Chai, and M. Elkashlan, "Active RIS versus passive RIS: Which is superior with the same power budget?" *IEEE Communications Letters*, vol. 26, no. 5, pp. 1150–1154, 2022.

[40] O. I. M. A. P. Prudnikov, Y. A. Brychkov and R. H. Romer, *Integrals and Series, Vol. 3: More Special Functions*. Amsterdam: Gordon and Breach Science Publishers, 1986.